Icarus 273 (2016) 296–314

Contents lists available at ScienceDirect

Icarus

journal homepage: www.elsevier.com/locate/icarus

Complex explosive volcanic activity on the Moon within Oppenheimer crater

Kristen A. Bennett[a,*], Briony H.N. Horgan[b], Lisa R. Gaddis[c], Benjamin T. Greenhagen[d], Carlton C. Allen[e], Paul O. Hayne[f], James F. Bell III[a], David A. Paige[g]

[a] School of Earth and Space Exploration, Arizona State University. ISTB4 Room 795, 781 Terrace Mall, Tempe AZ 85287, United States
[b] Department of Earth, Atmospheric, and Planetary Sciences, Purdue University, 550 Stadium Mall Drive, West Lafayette, IN 47907, United States
[c] Astrogeology Science Center, U.S. Geological Survey, 2255 N. Gemini Drive, Flagstaff, AZ 86001, United States
[d] Johns Hopkins University Applied Physics Laboratory, 11100 Johns Hopkins Rd, Laurel, MD 20723, United States
[e] NASA Johnson Space Center, Emeritus, 2101 NASA Road 1, Houston, TX 77058, United States
[f] NASA Jet Propulsion Laboratory, 4800 Oak Grove Dr, Pasadena, CA 91109, United States
[g] Department of Earth, Planetary, and Space Sciences, University of California, Los Angeles, 595 Charles E Young Dr E, Los Angeles, CA 90095, United States

ARTICLE INFO

Article history:
Received 27 July 2015
Revised 10 December 2015
Accepted 3 February 2016
Available online 10 February 2016

Keywords:
Volcanism
Spectroscopy
Infrared observations
Mineralogy
Moon
Moon, surface

ABSTRACT

Oppenheimer crater is a floor-fractured crater located within the South Pole–Aitken basin on the Moon, and exhibits more than a dozen localized pyroclastic deposits associated with the fractures. Localized pyroclastic volcanism on the Moon is thought to form as a result of intermittently explosive Vulcanian eruptions under low effusion rates, in contrast to the higher-effusion rate, Hawaiian-style fire fountaining inferred to form larger regional deposits. We use Lunar Reconnaissance Orbiter Camera images and Diviner Radiometer mid-infrared data, Chandrayaan-1 orbiter Moon Mineralogy Mapper near-infrared spectra, and Clementine orbiter Ultraviolet/visible camera images to test the hypothesis that the pyroclastic deposits in Oppenheimer crater were emplaced *via* Vulcanian activity by constraining their composition and mineralogy. Mineralogically, we find that the deposits are variable mixtures of orthopyroxene and minor clinopyroxene sourced from the crater floor, juvenile clinopyroxene, and juvenile iron-rich glass, and that the mineralogy of the pyroclastics varies both across the Oppenheimer deposits as a whole and within individual deposits. We observe similar variability in the inferred iron content of pyroclastic glasses, and note in particular that the northwest deposit, associated with Oppenheimer U crater, contains the most iron-rich volcanic glass thus far identified on the Moon, which could be a useful future resource. We propose that this variability in mineralogy indicates variability in eruption style, and that it cannot be explained by a simple Vulcanian eruption. A Vulcanian eruption should cause significant country rock to be incorporated into the pyroclastic deposit; however, large areas within many of the deposits exhibit spectra consistent with high abundances of juvenile phases and very little floor material. Thus, we propose that at least the most recent portion of these deposits must have erupted *via* a Strombolian or more continuous fire fountaining eruption, and in some cases may have included an effusive component. These results suggest that localized lunar pyroclastic deposits may have a more complex origin and mode of emplacement than previously thought.

1. Introduction

Over 100 pyroclastic or "dark mantling" deposits have thus far been identified on the Moon (Gaddis et al., 1985, 2003; Hawke et al., 1989; Carter et al., 2009; Gustafson et al., 2012; Campbell et al., 2014). These deposits are characterized by their low albedo and are believed to be products of explosive volcanic eruptions.

Pyroclastic deposits are high priority targets for future exploration because of both their scientific value and their potential as a resource. Lunar pyroclastic materials are thought to originate from deep within the Moon. Therefore their primitive composition may help to constrain the composition and geophysical evolution of the lunar magma ocean and the lunar mantle (Delano, 1986; Shearer and Papike, 1993). Pyroclastic glass beads returned as Apollo samples have surface coatings that indicate that they formed in volatile-rich eruptions, and recent reanalysis of the Apollo 17 glass beads revealed melt inclusions with water content as high as the Earth's mantle (Hauri et al., 2011). The

* Corresponding author. Tel.: +1 8052168887.
E-mail address: kristen.a.bennett@asu.edu (K.A. Bennett).

http://dx.doi.org/10.1016/j.icarus.2016.02.007
0019-1035/

abundance and source of these volatiles may have major implications for the interior structure, composition, and origin of the Moon (Hauri et al., 2015). Pyroclastic deposits are also likely targets for future *in situ* resource extraction, due to both their high abundances of metal oxides that could be processed to yield oxygen in higher abundances than any other known lunar material (Allen et al., 1996), and their thickness and uniform grain size, which could facilitate rapid extraction of ^{3}He (Hawke et al., 1990). Indeed, Burns et al. (2013) proposed a landing site near the Schrodinger pyroclastic deposit as a potential location for a future lunar mission.

Lunar pyroclastic deposits are generally divided into localized (<1000 km^2 in area) and regional (>1000 km^2 in area) deposits (*e.g.,* Gaddis et al., 2003). The localized deposits that have been investigated previously using Earth-based telescopic spectra appear to contain minerals likely to originate from different sources, including juvenile magmatic minerals (typically clinopyroxenes, olivine and/or quenched glass) and local country-rock (orthopyroxenes from lunar highlands or clinopyroxenes from mare; Hawke et al., 1989) or mixtures of these. However, the juvenile component of localized deposits is poorly constrained, as both olivine and glass could account for the spectral shapes observed (Gaddis et al., 2000). Strombolian activity is not energetic enough to strip country rock from the vent walls to produce deposits with non-juvenile components. Fire fountaining could erode the vent wall enough to incorporate non-juvenile material, but this implies such high eruption rates that the ejected pyroclasts would be hot enough that they would coalesce to form lava flows instead of forming pyroclastic deposits (Head and Wilson, 1979). Therefore, localized deposits are primarily thought to result from Vulcanian-style periodic eruptions. Vulcanian eruptions occur when intruding magma near the surface solidifies and creates a plug. The magma in the conduit is trapped below this plug; as gas exsolves from the magma, pressure builds up under the plug. Once the pressure overcomes the strength of the plug the magma explodes violently, ejecting juvenile magmatic material and up to 50% country rock (*e.g.,* Head and Wilson, 1979). Vulcanian-style eruptions imply a relatively low mass eruption rate (*e.g.,* Head and Wilson, 1979; Gaddis et al., 2000), as would be the case for extrusion through crustal weak points from sills and dikes (Head and Wilson, 1979; Head et al., 2000). This scenario is supported by the association of small deposits with floor-fractured craters (*e.g.*, Schultz, 1976). Floor-fractured craters are thought to occur when a sill intrudes beneath a crater and the increased pressure causes the crater floor to uplift and fracture. The magma in the sill can then slowly travel through these fractures and reach the surface with a low mass eruption rate (Head and Wilson, 1979; Jozwiak et al., 2015). Dozens of previously unrecognized localized pyroclastic deposits have been identified in the past decade using Clementine data (Gaddis et al., 2003), LROC visible images (Gustafson et al., 2012), and radar signatures (Carter et al., 2009; Campbell et al., 2014), resulting in what is now a global population of more than 100 hypothesized local and regional pyroclastic deposits.

Regional pyroclastic deposits are thought to result from either low mass eruption rate Strombolian eruptions (coalesced bubble explosions) or high mass eruption rate fire fountains (Heiken et al., 1974; Wilson and Head, 1981). The regional deposits may be related to mare volcanism, as they are often associated with rilles and vent-like irregular depressions on mare margins (Head, 1974; Gaddis et al., 1985). Regional deposits consist of more juvenile material than would be expected in Vulcanian deposits, and contain both glass and partially crystalline beads (Gaddis et al., 1985). Volcanic glass is formed when erupted magma droplets occur in an optically thin part of a fountain and are quickly quenched, while crystalline beads are deposited when the droplets are in an optically thick part of the fountain and have time to crystallize before they cool (Arndt et al., 1984; Arndt and von Engelhardt, 1987). Glass and crystalline beads in a single eruption have been observed at Apollo 17 (*i.e.*, the Taurus–Littrow landing site) to have the same geochemical composition (Pieters et al., 1974), but this relationship has not been documented in detail for other regional pyroclastic deposits.

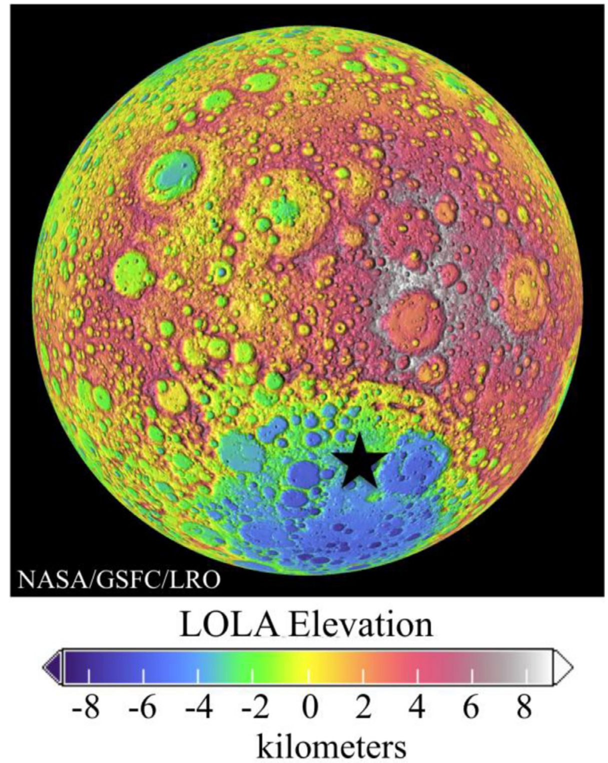

Fig. 1. LRO Lunar Orbiter Laser Altimeter lunar far-side topographic data (Smith et al., 2010) showing the global context of Oppenheimer crater (black star). Oppenheimer is located within the South Pole–Aitken basin.

Gaddis et al. (2013) identified at least 8 previously unrecognized sites of pyroclastic eruption in the floor of Oppenheimer crater using recently available high-resolution remote sensing data. This discovery increases the number of recognized volcanic vents in Oppenheimer crater to 15 and highlights the importance of pyroclastic volcanism in this and other floor-fractured craters. The presence of at least 15 pyroclastic deposits with a wide variety of sizes and morphologies within a single crater enables us to characterize the composition and occurrence of these deposits at a level not previously possible. In particular, we can assess the influence of local and regional factors such as crustal thickness, subsurface fractures, and crater rays on these volcanic deposits. In this study, we characterize the composition and morphology of the pyroclastic deposits within Oppenheimer crater using near- and thermal-infrared data and visible images from lunar orbiters to constrain the likely eruption style, mode of occurrence, and resource potential of each deposit.

2. Background

Oppenheimer crater is a floor-fractured crater located at 35°S and 166°W (Fig. 1) within the South Pole–Aitken basin (SPA). Oppenheimer is Pre-Nectarian (Hiesinger et al., 2012) and roughly 200 km in diameter. Fig. 1 shows the location of Oppenheimer crater and Fig. 3a shows the distribution of the largest pyroclastic deposits within the crater. The Oppenheimer pyroclastic deposits are associated with vents along fractures in the crater floor. The deposits range in size from 1500 km^2 (northwest deposit) to a few square kilometers (Gaddis et al., 2003, 2013). Most deposits are informally named here for their compass locations within the crater (*e.g.,* Oppenheimer south, Oppenheimer north, *etc.*). Although two of the deposits occur within formally named craters (Oppenheimer U and Oppenheimer H, respectively) on the floor of Oppenheimer, we will refer to these deposits by their compass locations (northwest and southeast) for consistency of naming with other deposits.

Compositional studies using Clementine UVVIS data at Oppenheimer crater showed little diversity between the pyroclastic deposits, suggesting that they had the same magmatic source, with a composition dominated by mafic minerals (*e.g.*, pyroxene) in fragmented basalts and very little, if any, volcanic glass (Petro et al., 2001). One eastern floor deposit showed a composition consistent with lunar highlands material, but this was interpreted to be due to relatively high-albedo impact ejecta lying over the eastern half of the crater. More recent work by Jawin et al. (2015) using Moon Mineralogy Mapper near-infrared spectra showed that several of the pyroclastic deposits within Oppenheimer exhibit signatures consistent with volcanic glass.

Although previous studies support an origin by Vulcanian eruption for all deposits in Oppenheimer (Head et al., 2000), the Oppenheimer northwest deposit (within and adjacent to the interior floor-fractured crater Oppenheimer U) could be large enough to be considered a regional deposit (Gaddis et al., 2003) and thus may have formed by the fire fountaining or Strombolian eruption style associated with regional deposits. Therefore, in this study we explore the possibility that the Oppenheimer northwest deposit formed *via* a different eruptive mechanism (fire fountaining/Strombolian), or that this deposit may be unique in that it is a large deposit with a Vulcanian origin (Gaddis et al., 2003).

We also note that the original efforts to classify lunar pyroclastic deposits selected arbitrary areas (2500 km^2, Gaddis et al., 2000; 1000 km^2, Gaddis et al., 2003) as the cutoff between regional and localized deposits. Oppenheimer northwest (1500 km^2) is only a few hundred square kilometers above the 1000 km^2 cutoff, and Oppenheimer south (674 km^2) is only a few hundred square kilometers below this cutoff (Gaddis et al., 2003). Although modeling studies on several deposits show that the size of a deposit generally correlates with its eruption mechanism (Gaddis et al., 2003), in this study we will not assume a particular eruption mechanism for a deposit solely based on its size, since several deposits are similar in size to the arbitrary cutoff.

Our analysis focuses on the compositions of the pyroclastic deposits as a way to distinguish between a fire fountaining or Strombolian *vs*. Vulcanian eruption style; fire fountaining and Strombolian activity should generally produce a deposit with more juvenile material and a more glass-rich composition. In this study, we test the prediction of compositional heterogeneity between the deposits using a variety of data. In contrast to previous studies, we utilize new spectral analysis methods that allow us to assess and map the relative glass content in these deposits. We use thermal- and near-infrared data in tandem, which yields more insight than separate analyses. Thermal infrared data are useful for deriving thermophysical properties and constraining the silicate composition of a material (Vasavada et al., 2012; Greenhagen et al., 2010). The thermal inertia yields information about the physical characteristics of a material; higher thermal inertia indicates blocky material while lower thermal inertia indicates finer grained particles. The Christensen Feature (CF) value, the emissivity maximum near 8 μm, constrains whether a material is dominantly composed of olivine, pyroxene or plagioclase, the major minerals on the lunar surface. However, the CF value cannot determine whether a material is crystalline or glassy. Also, CF values can be non-unique – for example, a material that is primarily pyroxene would have the same CF value as a material that is a mixture of olivine and plagioclase. Near infrared spectra are thus also used for improved detectability of several iron-bearing minerals (one cannot use near infrared spectra to easily detect an iron-poor mineral such as plagioclase). Near infrared spectra are also used to detect glass, which exhibits iron absorption bands at different wavelengths than more crystalline minerals (Section 4.2). Therefore, in this study we use near infrared data to help determine whether or not a pyroclastic deposit is glassy, and use thermal infrared data to constrain the composition of the glass. However, it is important to note that these infrared datasets only yield information on the composition and mineralogy of the surface of each deposit.

3. Eruption style and resulting deposits

Our aim in this study is to use the composition and mineralogy of the pyroclastic deposits to constrain the eruption style that produced the deposits (Vulcanian *vs*. Strombolian/fire fountaining) and thus to reconstruct the volcanic history of Oppenheimer crater. In Fig. 2, we illustrate several different types of eruptions and the resulting deposits. We discuss a single Vulcanian eruption, multiple Vulcanian eruptions, a Vulcanian eruption followed by a continuous Hawaiian-style eruption, and a single continuous eruption.

(1) *Single Vulcanian eruption:* Previous models suggest that deposits from Vulcanian eruptions should consist of both crystalline material that has a similar composition as the surrounding terrain and glassy or crystalline juvenile material (Head and Wilson, 1979). However, in considering the mechanics of a Vulcanian eruption, we hypothesize that it is necessary to invoke the concept of superposition and that the deposits may exhibit some stratification. In particular, the country rock and crystalline juvenile material that formed the initial plug should be located at the base of the pyroclastic deposit as it was the first material to be ejected. Due to break up of the solid plug, this initial deposit should be blocky at LROC resolution. Above this would be crystalline to glassy juvenile material that was ejected after the plug exploded. However, due to the rapid decrease in pressure once the overlying cap fails, an extended eruption of juvenile material is not expected in a purely Vulcanian eruption (Head and Wilson, 1979). Thus, we expect that the fine-grained overlying juvenile material should be a thin deposit, and that the blocky underlying crystalline juvenile material and country rock should be visible. At the resolution of our spectral datasets, this scenario would manifest as a mixture of country rock and juvenile material.

(2) *Multiple Vulcanian eruptions:* It is also possible that some vents experienced multiple cycles of Vulcanian activity. In this scenario, after the initial Vulcanian eruption, magma that was still slowly rising once again cooled to form a plug and increased the pressure in the conduit. The explosion caused by the overpressure in the conduit would create a deposit that is indistinguishable from a single Vulcanian eruption.

(3) *Vulcanian eruption followed by a continuous eruption*: If the initial Vulcanian eruption cleared the plug and the magma begins rising more rapidly, a continuous Hawaiian-style eruption could then take place. This would result in a layer of glass-rich juvenile material above the blocky Vulcanian deposit. Depending on how long this continuous eruption persists, the smooth glassy layer could completely obscure the underlying blocky material. The resulting deposit would either appear as glass-rich or glass-rich with some crystalline plug material and country rock.

(4) *Immediate continuous eruption:* In this scenario, there is no Vulcanian eruption. If magma reaches the surface at ascent rates higher than those expected to create Vulcanian

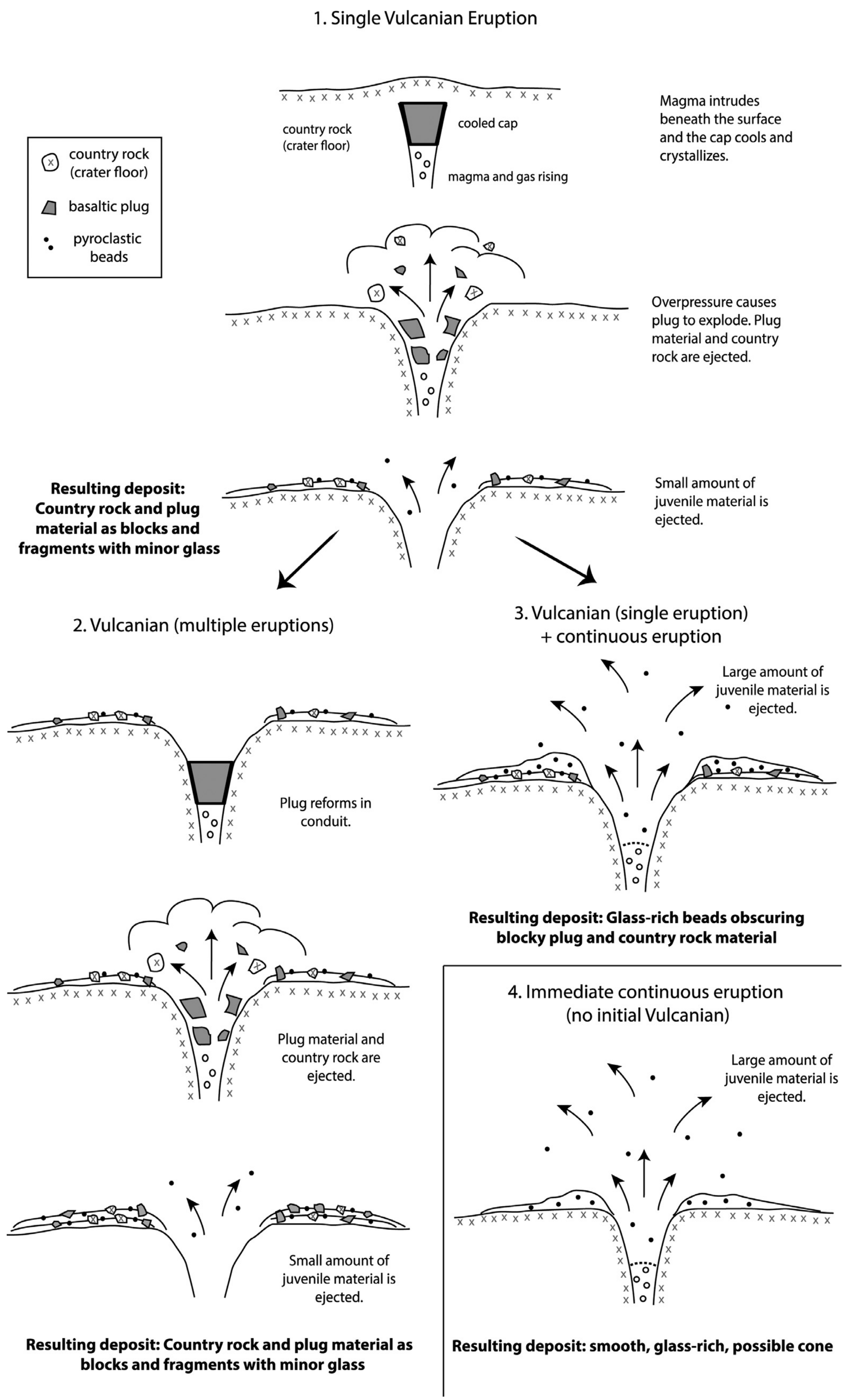

Fig. 2. Illustration of possible eruption styles and their resulting deposits.

eruptions, possibly emerging through fractures in the crater floor, a plug does not form and Hawaiian-style fire fountaining commences. The resulting deposit would be glass-rich and could form a small cone around the vent. This deposit is thus indistinguishable from a long-lived continuous eruption that started with a Vulcanian eruption but completely obscures the initial blocky deposit (scenario 3 above).

In Fig. 2 we illustrate that continuous fire fountaining would occur if a plug does not form in the conduit. However, it is also possible that Strombolian activity could occur if the mass eruption rate is low enough. The resulting deposit from a Strombolian eruption would be glass-rich and therefore indistinguishable from fire fountaining deposits in this study. Modeling efforts outside the scope of this study would be necessary to distinguish between Strombolian and fire fountaining activity.

4. Methods

In this study we use a variety of remote sensing datasets to study the Oppenheimer crater pyroclastic deposits and their environs, including thermal-infrared data from the Diviner Lunar Radiometer Experiment (Diviner; Paige et al., 2009) on the Lunar Reconnaissance Orbiter (LRO) and visible to near-infrared (VNIR) hyperspectral images from the Moon Mineralogy Mapper (M^3; Pieters et al., 2009; Green et al., 2011) on Chandrayaan-1. We also include LRO Lunar Reconnaissance Orbiter Camera (LROC; Robinson et al., 2010) visible images and Clementine ultraviolet to visible color ratio maps for context (Nozette et al., 1995).

4.1. LRO Diviner thermal-infrared datasets

We derive silicate composition, iron abundance, and the thermal inertia of Oppenheimer crater and its pyroclastic deposits from Diviner thermal-infrared data (Paige et al., 2009). We investigate the silicate mineralogy of Oppenheimer through an analysis of the infrared emissivity maximum, or the Christiansen Feature (CF; Greenhagen et al., 2010). The CF value is the wavelength location of the emissivity maximum (or reflectance minimum), which occurs near 8-μm, but is strongly dependent upon the degree of polymerization of minerals, with framework silicate minerals such as feldspars exhibiting CFs at shorter wavelengths than less polymerized pyroxene and olivine. The Diviner instrument has three channels (3–5) near 8-μm that we use to estimate the CF value. The parabola that fits the three emissivity values from channels 3 to 5 is calculated, and the wavelength that corresponds to the maximum of that parabola is estimated as the CF value. For a more detailed explanation of calculating CF values, see Greenhagen et al. (2010). We use Diviner CF values to search for relative abundances of silicate phases such as plagioclase (Glotch et al., 2010) that near-infrared spectra often cannot detect, which could indicate mixing with country rock in Vulcanian-style eruptions.

In order to evaluate the variability of CF values within each deposit and to determine the CF value for the glassiest portion of each deposit, we report CF values for several different regions of interest. To obtain the average CF value of each pyroclastic deposit, we created a region of interest for each deposit by outlining the extent of the deposit using visible images and then took the average CF value of each region. To obtain the maximum CF value of a deposit, we visually identified areas within each deposit that exhibited higher CF values than the rest of the deposit and took the average CF of those areas. Not every deposit exhibited areas with enhanced CF values. We also obtained the CF value for glass-rich areas of each deposit by averaging the CF value of all pixels within each deposit that exhibited an M^3 glass band depth above a threshold value. Finally, the CF values for the crater floor were obtained by averaging a section of each side of the crater floor away from the pyroclastic deposits.

We also use Diviner data to estimate iron abundances of lunar pyroclastic deposits. Allen et al. (2012) found that the bulk FeO wt% of Apollo soil samples correlated with the CF value ($FeO = 74.24*CF - 599.9$; $r^2 = 0.90$). We use this relationship between FeO abundance and CF values for lunar glasses to estimate the FeO wt% of each deposit (Allen et al., 2012).

Finally, we use Diviner thermal-infrared data to derive the thermal inertia of each deposit, $I = \sqrt{k\rho c_p}$, where k is thermal conductivity, ρ is density, and c_p is heat capacity. We parameterize thermal inertia through the "H-parameter", which describes the scale depth of exponential increase, *e.g.*, $\rho(z) \sim e^{-z/H}$. Thermal conductivity is assumed to be proportional to density, and therefore follows the same exponential depth increase. The boundary values on conductivity and density are those of Vasavada et al. (2012), with the exception of the surface density, which is $\rho_d = 1100\,\mathrm{kg\,m^{-3}}$. For each map element, we perform a least-squares minimization on the nighttime regolith temperatures from Diviner, to derive the H-parameter. The H-parameter is inversely related to thermal inertia, with larger H values indicate lower thermal inertia within the upper ~10 cm. Regional lunar pyroclastic deposits typically exhibit lower nighttime temperatures than the lunar regolith, which implies that they have lower thermal inertia (Bandfield et al., 2011) and can yield insight on the particle sizes and shapes in the deposits. For example, spherical pyroclastic beads of juvenile material could stack in an organized way creating more pore space and lowering the thermal inertia, while deposits with higher country rock content could have a thermal inertia similar to the average lunar regolith.

4.2. M^3 visible to near-infrared spectral maps

We use M^3 visible to near-infrared spectra (0.43–3.0 μm) to characterize the iron-bearing minerals and glasses within Oppenheimer crater. M^3 Level 2 reflectance data from the global mapping campaign is acquired from the Planetary Data System, which includes corrections for thermal emission as well as topographic, photometric, and instrumental effects (Green et al., 2011; Clark et al., 2011; Hicks et al., 2011; Boardman et al., 2011; Besse et al., 2013). Here we use two images from high signal to noise ratio (SNR) operational periods (M3G20090621T022743 and M3G20090621T065503), which cover the eastern half of the crater, and two images from low SNR operational periods (M3G20090815T074952 and M3G20090718T101402;), which cover the west and the northeast rim of the crater. All images are from the "2C" period of the mission when the spacecraft operated from a higher orbit, so the native resolution of all four images is ~280 m/pixel (two times lower resolution than the global data from earlier in the mission). There is a coverage gap between these images (Figs. 4 and 5). There is no M^3 coverage over part of the western half of Oppenheimer crater where the centers of the northwest and southwest pyroclastic deposits are located. These images are mapped into a mosaic with a local cylindrical projection at 140 m/pixel horizontal resolution (Figs. 4 and 5).

Iron-bearing minerals can be identified in M^3 data based on the position and shape of the 1 and 2 μm iron absorption bands, which vary significantly with mineralogy and composition (*e.g.*, Adams, 1974; Cloutis and Gaffey, 1991; Sunshine and Pieters, 1993; Horgan et al., 2014). See Fig. S4 for examples of near-infrared spectra of iron-bearing minerals typically found on the Moon. The wavelength range of M^3 covers both of the broad 1 and 2 μm absorption bands, and the 82 spectral band global dataset is ideal in particular for analysis of the 1 μm band, with 2× higher spectral sampling in the 0.7–1.6 μm region.

Before the 1 and 2 μm iron absorption bands can be analyzed in detail, however, the overall continuum slope must be suppressed by removing an approximate continuum function. In analyzing a wide variety of lunar terrains, we find that the simplest continuum shape that fits most lunar spectra is a linear convex hull, where linear continua are found independently over the 1 and 2 μm band regions (*e.g.*, Clark and Roush, 1984). To find the continuum function, we first smooth each spectrum with nested boxcar average and median smoothing functions, both 3 channels wide. Then, we remove an initial estimate of the continuum, fit to fixed endpoints at 0.7, 1.5, and 2.6 μm. Next we fine-tune these endpoints for each spectrum by finding the local maxima in this initial continuum removed spectrum. For the 1 μm region, we find the local maxima between 0.6–1.0 and 1.0–1.7 μm, which become the new endpoints. For the 2 μm region, local maxima are found between the previous endpoint (between 1.0 and 1.7 μm) and 2.0 μm and 2.0–2.6 μm. These ranges avoid both possible long-wavelength plagioclase absorptions near 1.3 μm and thermal effects beyond 2.6 μm. Using the new endpoints, the final continuum of three joined linear segments is calculated from the original spectrum.

We use the methods of Horgan et al. (2014) to map the position of the 1 and 2 μm iron absorption bands, which are indicators of iron mineralogy. Band position is parameterized as band center, calculated as the wavelength position of the minimum of a fourth-order polynomial fit to the spectrum within 0.1 μm of the minimum channel in each band. Band depth is the percent depth below the continuum at the location of the band center (*i.e.*, one minus the value of the continuum removed spectrum at that wavelength). The 1 and 2 μm band positions together can be used to broadly distinguish between orthopyroxene (OPX; band centers between 0.9–0.94 and 1.8–1.95 μm), clinopyroxene (CPX; 0.98–1.06 and 2.05–2.4 μm), and iron-bearing glass (1.06–1.2 and 1.9–2.05 μm). Mixtures of these minerals have band centers that fall in the intermediate regions between the endmembers (Horgan et al., 2014). Other iron-bearing minerals can also be identified using similar methods. Olivine exhibits a characteristically asymmetric 1 μm band typically centered near 1.05–1.08 μm and plagioclase feldspars exhibit broad and shallow bands centered between 1.25 and 1.35 μm, but neither exhibits a corresponding 2 μm band.

One drawback of only using band centers when trying to identify glass in a mixture is that glass is a poor absorber compared to other iron-bearing minerals, and thus glass only significantly shifts the 1 and 2 μm band centers when it is present at very high abundances (typically 50–80 wt%; Horgan et al., 2014). However, low to moderate glass abundances can still cause additional absorption beyond 1.1 μm, where other minerals are not as strongly absorbing. Thus, we have developed a “glass band depth” spectral parameter to aid in identifying glass at lower abundances, which is equal to the average of the depth below the continuum at three wavelengths: 1.15, 1.18, and 1.20 μm. This parameter will detect glass, but will also detect olivine if present.

4.4. Additional data sets

We use LROC wide angle camera (WAC) mosaics and narrow angle camera (NAC) images to provide context for our composition and mineralogy study (Robinson et al., 2010). We use the global WAC mosaic available on JMARS for the Moon (Christensen et al., 2009) and individual calibrated NAC images that are currently available from the PDS. These LROC products are used to study the morphology and albedo variations of pyroclastic deposits within Oppenheimer crater.

We also use Clementine color ratio maps that are publicly available on JMARS for the Moon (McEwen, 1997; Christensen et al., 2009). In Clementine color ratio maps, red is 750/415 nm, green is 750/950 nm, blue is 415/750 nm. These maps cancel out the dominant brightness variations from albedo and topography and highlight color differences dues to mineralogy and maturity. We use these maps to provide context for Oppenheimer, especially with respect to the influence of crater ejecta and rays on observed remote sensing signatures.

5. Results

5.1. Diviner results

Fig. 3b shows the CF map of Oppenheimer crater and Table 1 shows the average CF value of each pyroclastic deposit as well as the crater floor. Observed CF values range from roughly 8.15–8.40 μm, with much of the crater floor showing comparable values to nearby highlands, at 8.15–8.2 μm. All pyroclastic deposits have a higher CF value than the crater floor, but the large western pyroclastic deposits (south, southwest, northwest) exhibit higher CF values (8.28–8.33 μm, with areas of enhanced CF values that reach as high as 8.48 μm) than the smaller eastern deposits (north, east, southeast, south–southeast; 8.25–8.27 μm). This may or may not be related to the observation that the western crater floor also has a higher CF than the eastern crater floor. A fresh impact crater (indicated by the arrow in Fig. 3c) near the north pyroclastic deposit has the lowest CF value in the study area (8.07 μm). We converted the Diviner CF values to FeO wt% (Table 1). Since iron abundance correlates with CF values, the same trends observed in the CF values apply to the FeO wt%. The western pyroclastic deposits have an FeO abundance of 15–19 wt%, while the eastern pyroclastic deposits have 13–14%. The areas of enhanced CF within the northwest, southwest and south deposits have FeO abundances of 30 ± 11, 23 ± 6, and 26 ± 10 wt%, respectively.

Fig. 3c shows the *H*-parameter (the inverse of thermal inertia) of Oppenheimer crater. The thermal inertia calculations presented here do not fully account for slope variations, which is why the crater walls and rim are apparent in Fig. 3c. As we are primarily interested in the crater floor and pyroclastic deposits, where slopes are small, this does not strongly affect our results. The crater floor and the pyroclastic deposits have *H*-parameter values ranging from 0.08 to 0.10, and the *H*-parameter value for each pyroclastic deposit is the same as its surrounding crater floor material. The largest variation in thermal inertia is the small, fresh impact crater near the northern pyroclastic deposit that has an *H*-parameter value of −0.2 (arrow in Fig. 3c; also see Table 1). Fresh impact craters usually exhibit higher thermal inertia values, and therefore lower *H*-parameter values, due to the high abundance of small rocks in the ejecta. The negative value at the fresh crater implies that the thermal inertia in the upper ~10 cm is higher than the maximum value allowed by the standard model (~90 $J\,m^{-2}\,K^{-1}\,s^{-1/2}$). A different model, with higher limiting thermal inertia, would be needed to accurately describe this area. Apart from this fresh impact crater, the largest variation in thermal inertia is between the higher *H*-parameter (lower thermal inertia) western half of the crater floor and the lower *H*-parameter (higher thermal inertia) eastern half.

5.2. M^3 results

Fig. 4 shows the M^3 glass band depth parameter across Oppenheimer crater and Fig. 5 shows an RGB composite of these three maps, with the red channel corresponding to the glass band depth parameter, the green channel the 1 μm band center (see Fig. S1), and the blue channel the 2 μm band center (see Fig. S2). In this color scheme, we interpret that glass-rich areas are yellow, CPX and glass mixtures are magenta, OPX-dominated areas are green, and CPX/OPX mixtures are teal or blue. See Table S1 in the Supplementary material for more details about this color scheme.

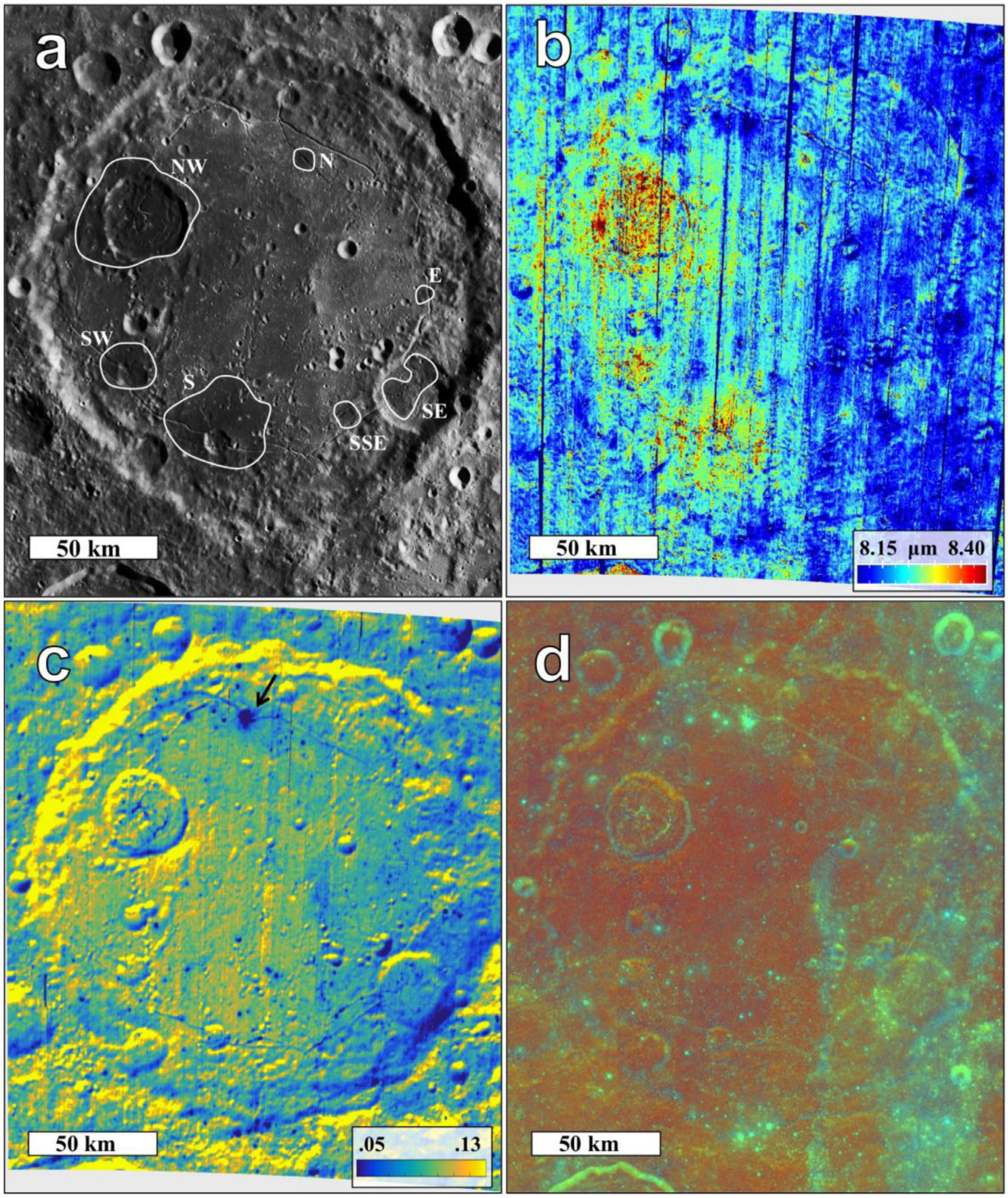

Fig. 3. (a) LROC WAC mosaic of Oppenheimer crater from the global mosaic available on JMARS for the Moon (Robinson et al., 2010; Christensen et al., 2009). The 7 largest pyroclastic deposits are outlined and labeled. (b) Diviner CF map of Oppenheimer crater. (c) *H*-parameter (inverse thermal inertia) of Oppenheimer crater. The black arrow points to a fresh crater. (d) Clementine color ratio of Oppenheimer crater available on JMARS for the Moon (McEwen et al., 1997; Christensen et al., 2009). The light green terrain in the eastern part of Oppenheimer is hypothesized to be a crater ray. (For interpretation of the references to color in this figure legend, the reader is referred to the web version of this article.)

Analysis of M^3 spectra shows clear spectral differences between the crater floor and the pyroclastic deposits, as well as within and between the various pyroclastic deposits. All reported band center ranges reported here are one standard deviation on either side of the mean, for spectra with 1 and 2 μm band depths greater than 2%. Fig. 6a shows a density plot of the 1 and 2 μm band centers of the crater, along with approximate ranges for OPX, CPX, and glass-dominated spectra based on our local analyses. The densest portion of Fig. 6a corresponds to the crater floor, which tends to fall both within the OPX field and between the OPX and CPX fields. This general range encompasses both the lateral and vertical diversity in the composition of the crater floor. The eastern half of the crater floor exhibits 1 and 2 μm band centers between 0.90–0.98 and 1.99–2.06 μm, consistent with an OPX/CPX mixture. The western crater floor exhibits similar 1 μm band centers but 2 μm band centers shifted lower, between 1.93 and 2.02 μm. Many crater walls, fracture walls, and fresh craters in the eastern crater floor also exhibit shifted band centers, typically between 0.91–0.94 and 1.96–1.99 μm. The west and central-eastern crater floor both exhibit small but positive values of the glass band depth parameter (1–3%).

In comparison, the pyroclastic deposits exhibit much larger values of the glass band depth parameter (3–8%). This makes the glass band depth parameter very useful for identifying

Table 1
Average Diviner-derived CF values, FeO, and thermal inertia for all deposits. Where deposits are large enough to exhibit significant variation, the maximum value for the CF and corresponding FeO are also shown in parentheses.

Deposit or unit	CF value (μm)	FeO (wt%)	Thermal inertia (*H*-parameter)
Pyroclastic deposits			
NW	8.33 ± 0.03 *(8.48 ± 0.15)*	19 ± 2 *(30 ± 11)*	0.10 ± 0.01
SW	8.31 ± 0.07 *(8.39 ± 0.08)*	17 ± 5 *(23 ± 6)*	0.10 ± 0.01
S	8.28 ± 0.06 *(8.43 ± 0.16)*	15 ± 4 *(26 ± 10)*	0.10 ± 0.01
SSE	8.25 ± 0.03	13 ± 2	0.08 ± 0.01
SE	8.25 ± 0.04	13 ± 3	0.08 ± 0.01
E	8.26 ± 0.04	13 ± 3	0.08 ± 0.01
N	8.27 ± 0.06	14 ± 4	0.10 ± 0.01
Non-pyroclastic deposits			
W crater floor	8.24 ± 0.03	12 ± 2	0.10 ± 0.01
E crater floor	8.20 ± 0.03	9 ± 2	0.08 ± 0.01
Fresh crater	8.07 ± 0.06	-1 ± 4	-0.20 ± 0.10

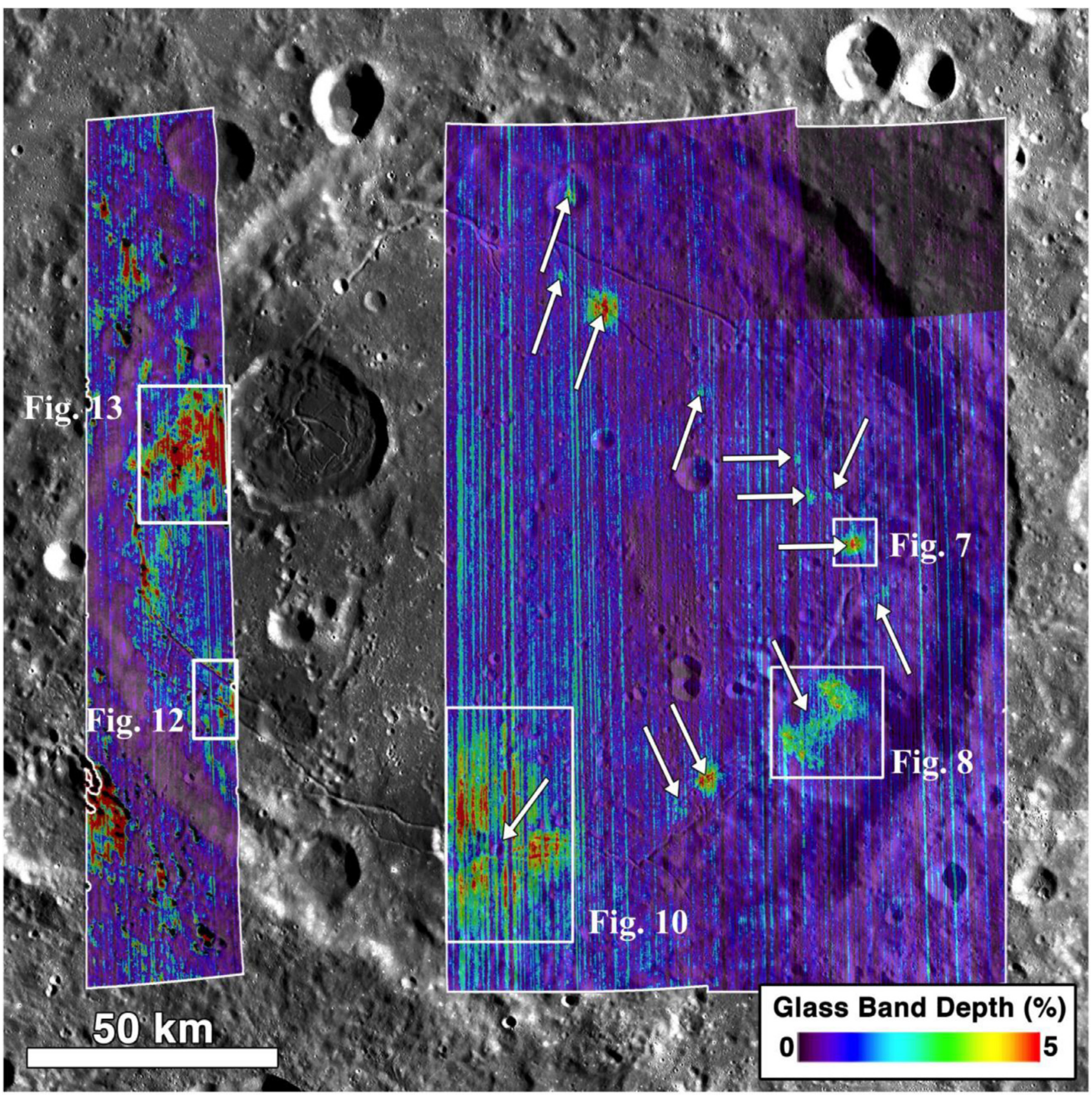

Fig. 4. M^3 glass band depth spectral parameter mapped in Oppenheimer crater, with LROC WAC mosaic from Fig. 3 as background. See Section 4.2 for M^3 image names. This spectral parameter indicates enhanced absorption between 1.15 and 1.20 μm in continuum removed spectra, consistent with glass. Arrows indicate sites of inferred pyroclastic deposits based on glass detections. Boxes indicate locations of deposits shown in detail in Figs. 7, 8, 10, 12 and 13. (For interpretation of the references to color in this figure, the reader is referred to the web version of this article.)

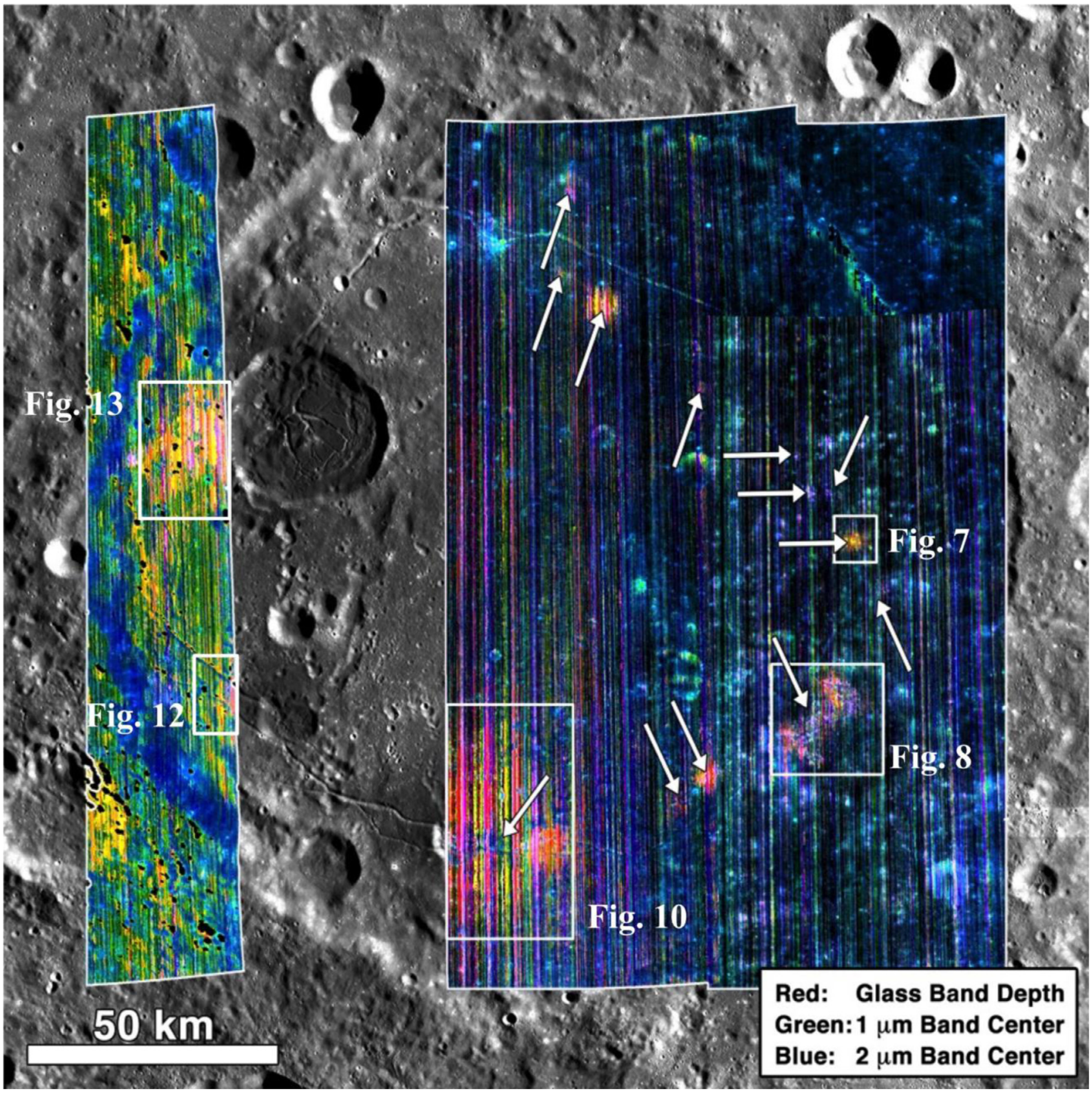

Fig. 5. M^3 RGB composite map of Oppenheimer crater, with LROC WAC mosaic from Fig. 3 as background. Red = glass band depth (Fig. 4; stretched from 0.1% to 3%), green = 1 μm band center (Fig. S1; stretched from 0.9 to 1.05 μm), blue = 2 μm band center (Fig. S2; stretched 1.95–2.25 μm). CPX mixed with glass is magenta, glass is yellow, OPX is green, OPX mixed with CPX is teal to blue (see Table S1 for more detailed explanation of color scheme). The five white boxes show the areas of additional figures where further analysis is presented. (For interpretation of the references to color in this figure legend, the reader is referred to the web version of this article.)

pyroclastic deposits, even deposits smaller than a few kilometers across. For example, the arrows in Fig. 4 point to 13 deposits that are detectable using the glass band depth parameters. There are also two larger deposits on the western side of the crater that are not entirely covered with M^3 data, which brings the total of pyroclastic deposits to 15 within Oppenheimer crater. This agrees with the number of pyroclastic deposits identified in Gaddis et al. (2013). However, the glass band depth parameter alone is not sufficient to uniquely identify glass, as it could also indicate olivine. We do not observe any spectroscopic evidence for olivine in the area, though, as all locations with greater glass band depths exhibit both longer wavelength 1 μm band centers and shorter wavelength 2 μm band centers. The shift to longer 1 μm band centers and shorter 2 μm band centers is apparent at the scale of the map in Figs. S1 and S2 in the Supplementary material. While olivine would be expected to shift the 1 μm band center to longer wavelengths, it would not be expected to shift the 2 μm band center at all. This shift in both bands is consistent with the presence of iron-bearing volcanic glass in Oppenheimer crater pyroclastic deposits (Horgan et al., 2014).

The spectral character of the central portions of the pyroclastics varies from glass-rich to CPX/glass mixtures. Only one deposit (south) exhibits signatures of OPX in its interior. An example of a glass-rich deposit is the east deposit, and a detailed analysis of this deposit is shown in Fig. 7. The plotted M^3 spectra show a progression from spectra consistent with an OPX/CPX mixture that is representative of the eastern crater floor (Fig. 7, spectrum 1) to the glass-rich pyroclastic materials (Fig. 7, spectrum 3). This progression is also shown by the clear linear trend in 1 and 2 μm band centers from those consistent with OPX/CPX mixtures to those consistent with glass in Fig. 6b. Indeed, the very high 1 μm band centers in this deposit (1.09–1.13 μm) are consistent with lab spectra of mixtures containing more than 70–80 wt% glass (Horgan et al., 2014).

In contrast, Fig. 8 shows a similar analysis of the southeast deposit, which we interpret as consisting of a mixture of CPX and glass. Fig. 9 shows LROC NAC images of this deposit for context (discussed in more detail in Section 4. 4). As indicated in Fig. 6c, many areas within this deposit exhibit 1 and, in particular, 2 μm band centers at longer wavelengths than the surrounding crater

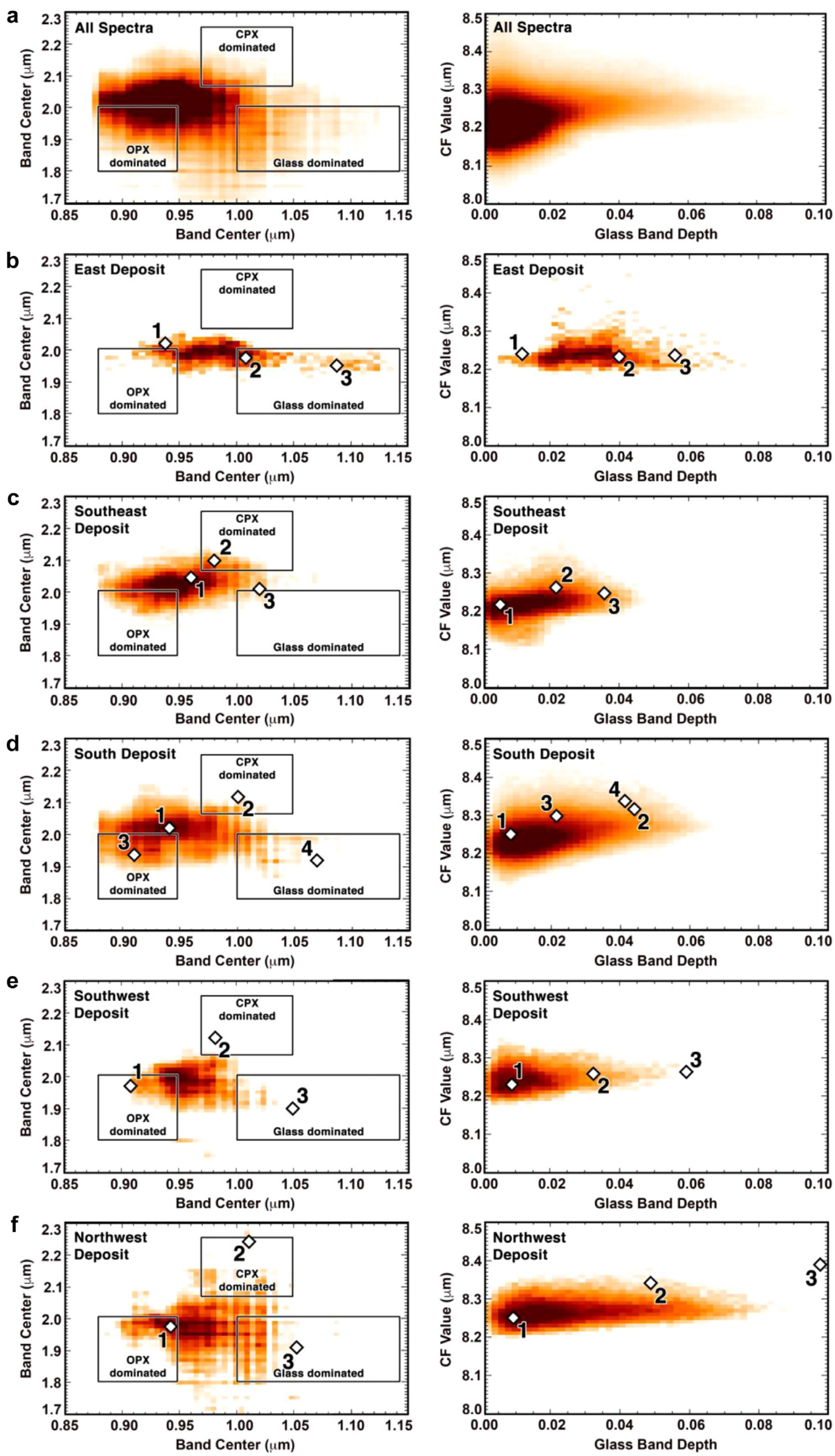

Fig. 6. Density plots illustrating spectral variability across the entirety of Oppenheimer Crater as well as within individual deposits. Darker orange colors indicate a higher density of spectra. The numbered points in each plot refer to spectra shown from each deposit in Figs. 7, 8, 10, 12, and 13. The left column shows M^3 1 and 2 μm band centers for all spectra with 1 μm band depths >5%, with parameter ranges expected for OPX, CPX and glass-dominated mixtures noted (Horgan et al., 2014). The right column shows Diviner CF values *vs.* M^3 glass band depths, and illustrates the relatively narrow range of CF values exhibited by glassy materials. (For interpretation of the references to color in this figure legend, the reader is referred to the web version of this article.)

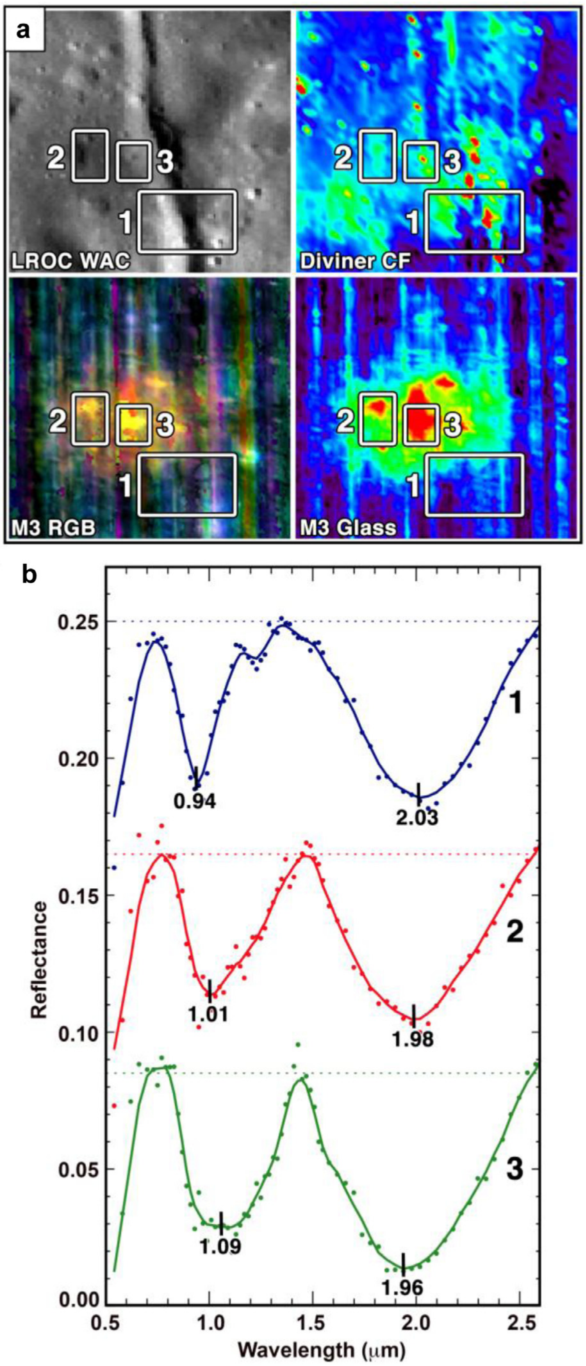

Fig. 7. Detailed analysis of the eastern deposit, as indicated in Fig. 4. This deposit is glass-rich, with no indication of significant CPX. (a) Enlarged maps of deposit from Figs. 3a and b, 4, and 5. (b) Continuum removed spectra, with calculated band centers noted.

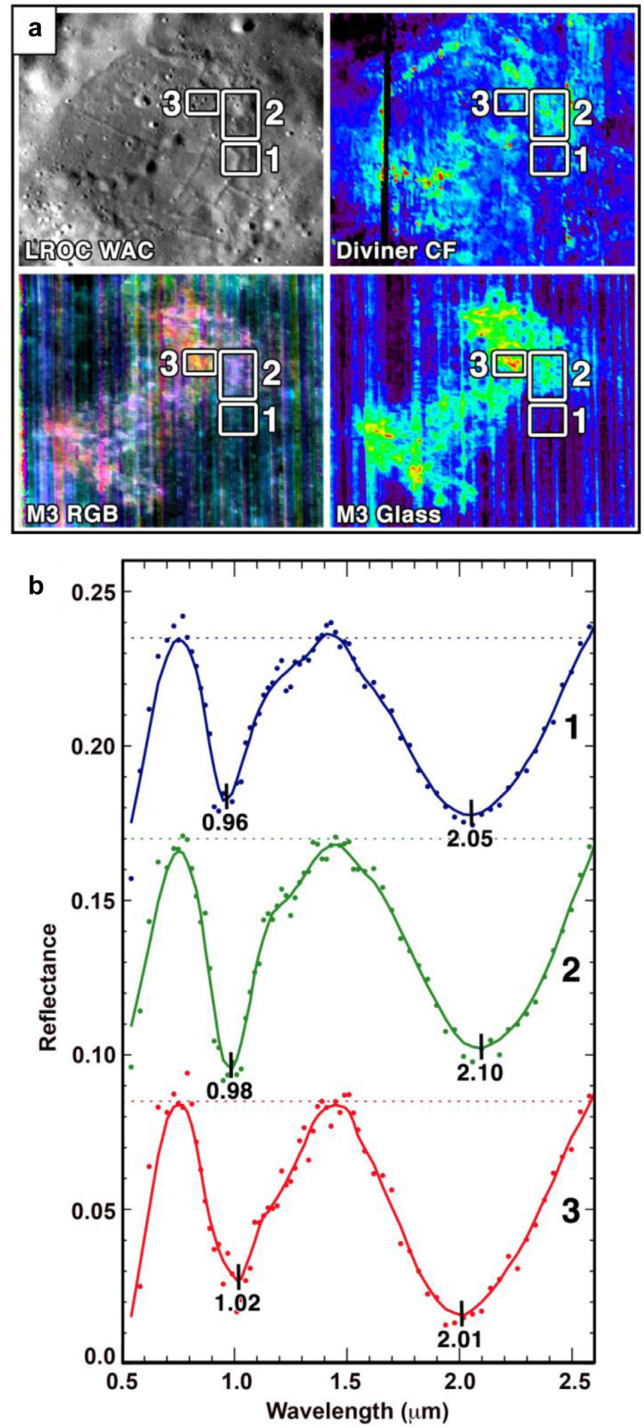

Fig. 8. Detailed analysis of southeastern deposit, as indicated in Fig. 4. This deposit is primarily a mixture of CPX and glass. See Fig. 7 caption for description of individual parts.

floor, which is consistent with the presence of CPX (Fig. 8, spectrum 2). However, these spectra also exhibit a shoulder on the 1 μm CPX band near 1.2 μm consistent with a glass component. While this shoulder could be due to a secondary CPX band that can occur in some very high Ca and/or Fe CPX (Klima et al., 2011; Trang et al., 2013), local context suggests that glass is more likely. Other areas within the deposit exhibit much stronger shoulders along with longer wavelength 1 μm band centers and shorter wavelength 2 μm band centers, all consistent with higher glass abundances, albeit still mixed with CPX (Fig. 8, spectrum 3).

The rest of the pyroclastic deposits in Oppenheimer crater vary from glass-rich to glass and CPX mixtures. Some deposits, such as the south deposit, show spectral variation within the deposit. In some areas, this deposit is glass-rich (Fig. 10, spectrum 4) and in others it is a CPX/glass mixture (Fig. 10, spectrum 2). Fig. 11 shows LROC WAC and NAC images of the south deposit for context (discussed in more detail in Section 4.4). This deposit also exhibits OPX signatures. A spectrum taken from a fracture within the south deposit is similar to the underlying OPX-rich crater floor (Fig. 10, spectrum 3), while central portions of the deposit are more

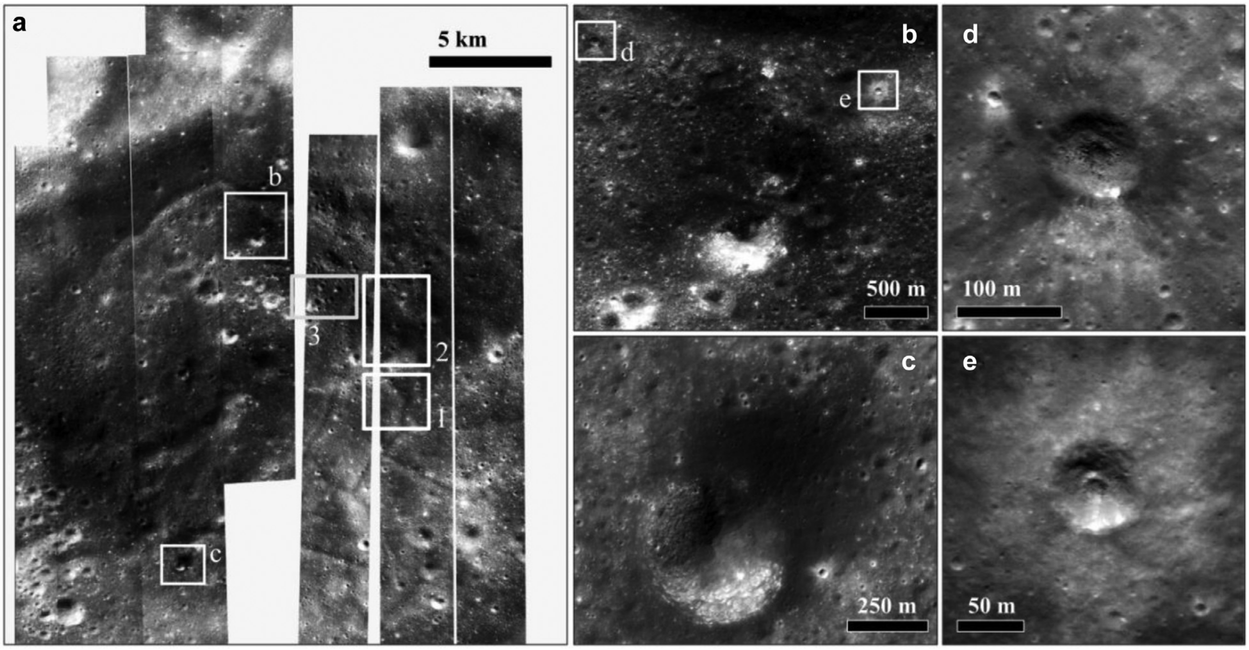

Fig. 9. (a) NAC mosaic of the SE deposit. Boxes labeled 1–3 show the location of spectra from Fig. 8. (b) (M171632283RE) and (c) (M1099924536RE) areas showing distinct low albedo mantling deposits within the SE deposit. (d, e) Bench craters within the SE deposits that indicate a bolide impacted into layered material, possibly loose pyroclastic material over a lava flow. The crater in (d) is ~85 m in diameter and the crater in (e) is ~65 m in diameter.

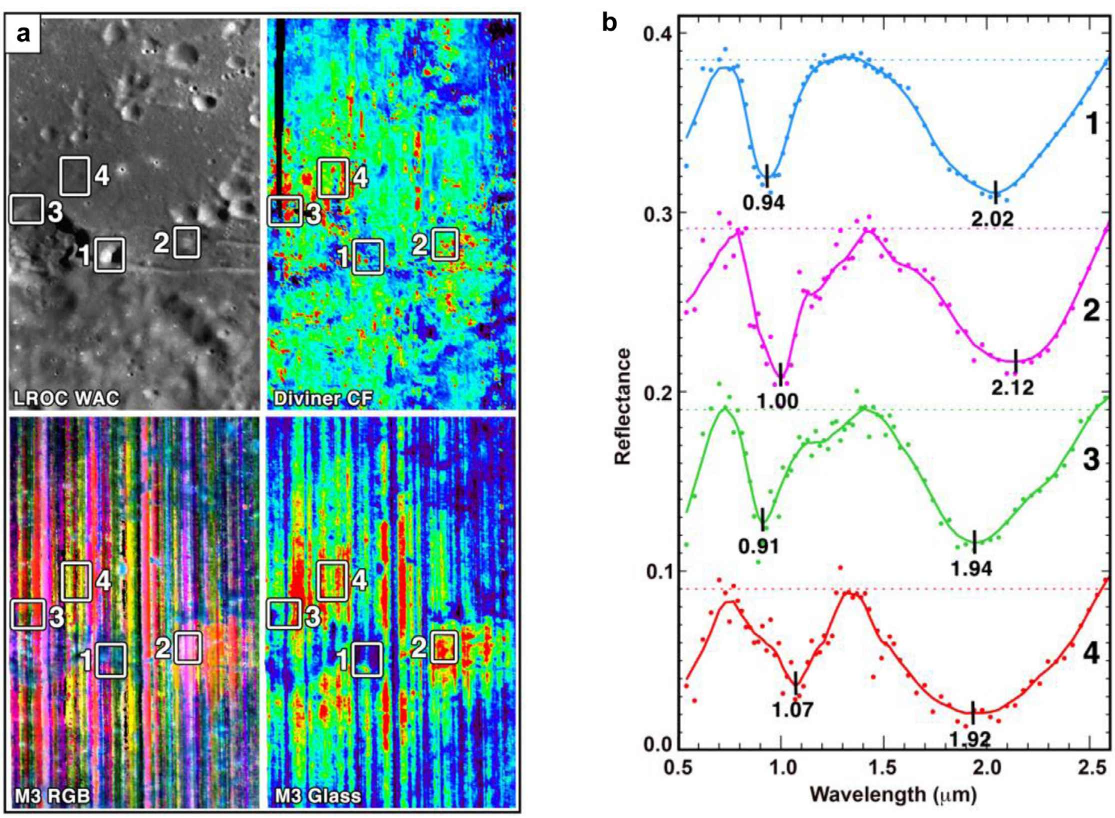

Fig. 10. Detailed analysis of complex southern deposit, as indicated in Fig. 4. This deposit exhibits glass-rich areas, CPX/glass mixtures, as well as OPX-rich country rock. See Fig. 7 caption for description of individual parts.

spectrally similar to the possible mixed OPX/CPX mantle in the eastern crater (Fig. 10, spectrum 1). In the south deposit in particular, significant striping of unknown origin (but presumed to be noise) in the M^3 data within the dark deposit makes highly local variability difficult to assess. However, there do appear to be real spectral variations between the main lobe and the eastern lobe of the deposit, with a more widely distributed CPX component to the east (Fig. 10, spectra 2 and 4). The available data over the northwest and southwest deposits, while also noisy, also appears to show variation in glass and CPX concentrations (Fig. 12).

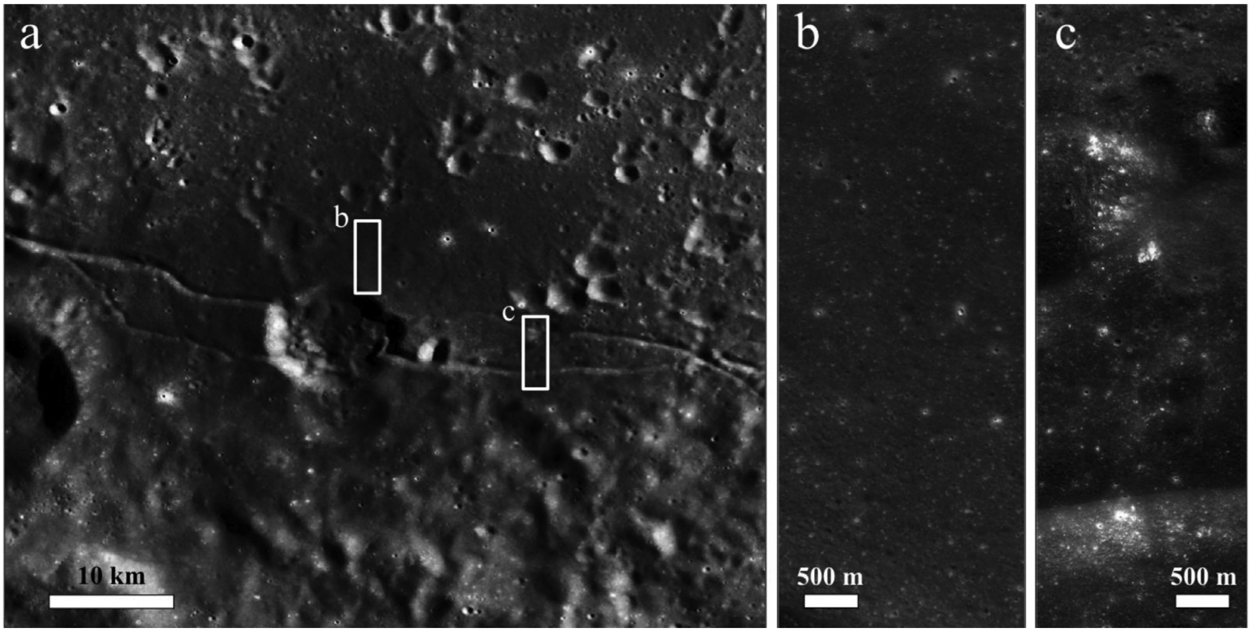

Fig. 11. (a) LROC WAC image of the S deposit. (b) NAC (M1119966094LE) of the glass-rich area that roughly corresponds to spectra 4 from Fig. 10. (c) NAC (M110316969RE) of the CPX-rich area that roughly corresponds to spectra 2 from Fig. 10. The depression in the top of the image could be a vent, the depression in the bottom part of the image is a fracture in the crater floor.

5.3. Synthesizing Diviner and M3

Fig. 6a shows a density plot comparing Diviner CF values and our M3 glass band depth parameter. While there is significant spread in CF values at low glass band depths (8.1–8.4 μm), the range in values shrinks with increasing glass band depths. In particular, CF values at glass band depths greater than 3% are restricted to greater than 8.2 μm. This trend of increasing CF value for increasing glass band depth is generally true at the scale of individual deposits as well, as is best shown in Fig. 6f for the northwest deposit. In this heterogeneous deposit, the glass-rich area that we sampled (Fig. 13, spectrum 3) exhibits very high CF values (Fig. 6f; glass band depth of ~0.10; CF value of ~8.40 μm). The CF values for the glassiest portions of each deposit are listed in Table 2. These results also show that the average CF values of each deposit are within the margin of error for the average CF values of the glass-rich portion of that deposit. Together, these observations suggest that the CF values tend to decrease away from the northwest deposit. The lowest CF values for the pyroclastics are observed in the glass-rich east deposit, where the CF values for the nearby crater floor and the glass-rich terrain are nearly identical. This implies that CF values are not strictly correlated with the glass content of a deposit, and thus are controlled by other factors.

6. Discussion

6.1. Crater ray

Petro et al. (2001) noted that there is a high albedo crater ray mantling the eastern half of Oppenheimer crater. This ray is apparent in several of our datasets, including the CF map (Fig. 3b) and Clementine color ratio (Fig. 3d). Because crater rays can contain both distal ejecta and local ejecta from secondary craters (*e.g.*, Hawke et al., 2004; Dundas and McEwen, 2007), it is important to know whether the ray was emplaced before or after the pyroclastic deposits. If the ray was emplaced afterwards, we must account for this in our interpretations. Fig. 14 shows a Clementine color ratio map of part of the far side of the Moon. Oppenheimer is circled and the ray crossing Oppenheimer is outlined. There are several craters that this ray may have originated from, including Jackson, Crookes, and Antoniadi. Jackson (22.4°N, 163.1°W) and Crookes (10.3°S, 164.5°W) craters are both Copernican aged and have visible rays (Wilhelms, 1987). Antoniadi crater (69.7°S, 172.0°W) is late Imbrium aged, and therefore we do not expect to see preserved rays (Wilhelms, 1987). However, there do appear to be a few rays extending from Antoniadi. It is possible that these rays are from a younger impact crater and they happen to cross Antoniadi. The rays from Jackson, Crookes, and near Antoniadi all are in line with the ray that mantles Oppenheimer crater, but we cannot determine which of these craters (if any) the ray over Oppenheimer was sourced from. However, craters that have bright, extensive rays are thought to be Copernican aged (such as Jackson and Crookes craters), while most lunar volcanism is thought to have stopped ~2 billion years ago (Hiesinger et al., 2000). Therefore we can safely assume that the ray postdates the pyroclastic deposits in eastern Oppenheimer crater. We will examine this possibility while interpreting our data.

6.2. Crater floor

M3 results showed that the ejecta covered crater floor exhibits band centers between 0.90–0.98 and 1.99–2.06 μm, consistent with an OPX/CPX mixture, but that the western (ray-free) half of the crater floor plus fracture walls and fresh craters on the crater floor have band centers shifted slightly lower. Together, these observations suggest that the actual crater floor is primarily OPX mixed with minor CPX. An OPX-rich composition of the floor of Oppenheimer crater is consistent with the general iron enhancement observed throughout the basin, likely due to the existence of OPX-bearing materials (*e.g.*, norite) across the South Pole–Aitken basin interior (Ohtake et al., 2014).

Both the western crater floor (8.24 μm) and the eastern crater floor (8.20 μm) have a CF value that is consistent with pyroxene, which is consistent with the M3 results. We hypothesize that the difference in CF value between the western and eastern crater floors is due to the large ray across the eastern half of the crater.

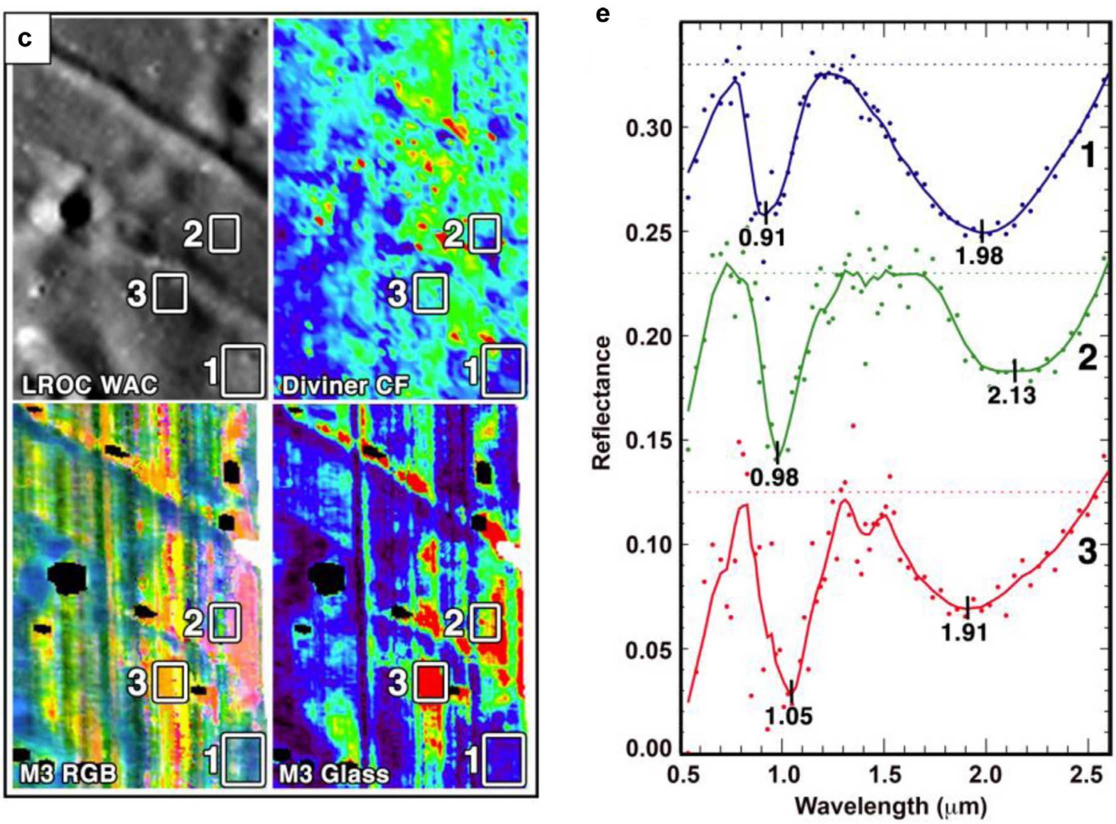

Fig. 12. Detailed analysis of the margin of the southwestern deposit that is covered by M^3 data, as indicated in Fig. 4. This deposit exhibits both glass-rich areas and CPX/glass mixtures. The M^3 scene covering this portion of the crater is from a warmer operational period and thus exhibits markedly greater noise than the scenes covering the eastern portion of the crater. See Fig. 7 caption for description of individual parts.

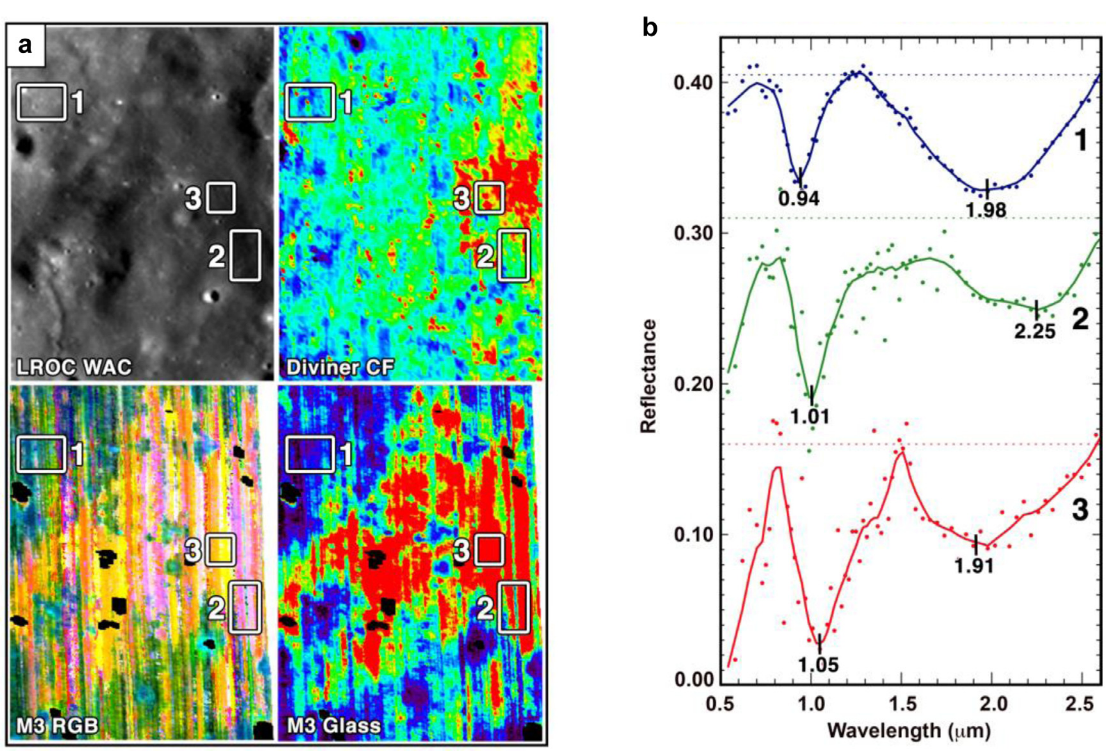

Fig. 13. Detailed analysis of the margin of the northwestern deposit that is covered by M^3 data, as indicated in Fig. 4. This deposit exhibits both glass-rich areas and CPX/glass mixtures. The M^3 scene covering this portion of the crater is from a warmer operational period and thus exhibits markedly greater noise than the scenes covering the eastern portion of the crater. See Fig. 7 caption for description of individual parts.

Table 2
Average CF values and derived FeO wt% for just the glassiest materials in each deposit. Glass is defined as having a 1 μm band center >1.0, 1 μm band depth >5%, a 2 μm band center <2.07, and elevated glass band depths, which are restricted to the highest available values in each deposit to isolate the glassiest materials. NW/SW deposits are only sampled in the more distal portions of the deposit that are covered by M^3.

Deposit	Average CF value of glass-rich pyroclastic materials	Standard deviation	FeO wt% of glass-rich pyroclastic materials	Standard deviation	Glass band depth range
NW	8.32	0.07	18	5	0.08–0.14
SW	8.27	0.04	14	3	0.05–0.08
S	8.28	0.05	15	4	0.07–0.09
SSE	8.28	0.07	15	5	0.05–0.08
SE	8.25	0.03	13	2	0.04–0.08
E	8.24	0.03	12	2	0.04–0.06
N	8.29	0.11	16	8	0.05–0.09

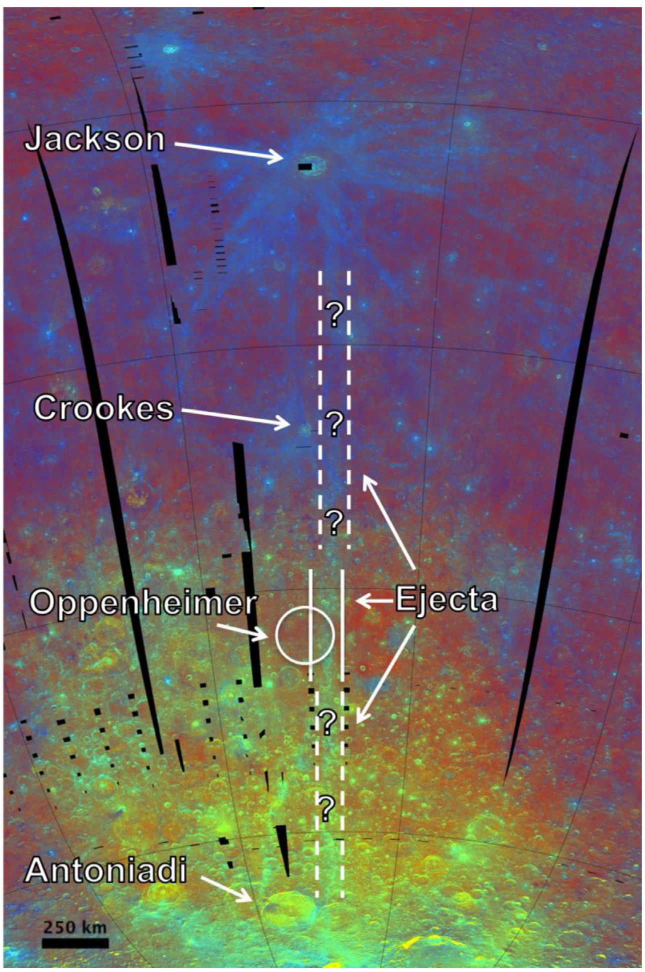

Fig. 14. Clementine color ratio map for the far side of the Moon (McEwen, 1997), showing the east central region of the South Pole–Aitken basin. Red is 750/415 nm, green is 750/950 nm, and blue is 415/750 nm. A lighter, ~linear feature is superimposed on the eastern portion of Oppenheimer crater, and this feature may be a crater ray. The thin black latitude and longitude lines are placed every 30°. Nearby craters include Jackson (located at 22.4°N, 163.1°W) and Antoniadi (located at 69.7°S and 172.0°W). (For interpretation of the references to color in this figure legend, the reader is referred to the web version of this article.)

Crater rays contain large numbers of secondary craters, which can churn up fresh material (Hawke et al., 2004; Dundas and McEwen, 2007). Since we observe a difference between the ray-covered east crater floor and ray-free west crater floor (8.20 μm and 8.24 μm, respectively), this could mean one of two things. One possibility is that the ray covered eastern half of the crater is more immature than the western half. Diviner CF is affected by maturity, so it is possible that the only difference between the two crater halves is how much space weathering has occurred, consistent with recent exposure of lower CF material inside of the crater ray in the eastern half. Another possibility is that the western crater floor is mantled by a material that is slightly more iron-rich than the OPX-rich crater floor. In this scenario, the entire crater floor could have been mantled by a thin layer of iron-rich material and this thin layer was overturned and mixed with crater floor material when the east half of the crater was impacted by the ejecta in the ray. The thin mantling layer could be pyroclastic material, as there are glass signatures on both the western and central-eastern crater floor in the M^3 mineral maps that could represent a small amount of pyroclastic glass.

6.3. Pyroclastic deposits

6.3.1. Thermal inertia

Previous studies have shown that regional pyroclastic deposits exhibit lower nighttime temperatures than the lunar regolith, which implies that they have a lower thermal inertia and are likely finer-grained than typical lunar regolith (*e.g.,* Bandfield et al., 2011). Our results (Fig. 3c; Table 1) are not consistent with those previous studies. The largest variation in thermal inertia is between the western half of the crater floor and the eastern half, which is covered by a large crater ray. The many secondary craters associated with the ray across the eastern half of the crater likely raises the thermal inertia of these areas. The pyroclastic deposits exhibit the same thermal inertia as the surrounding crater floor. The south, southwest, and northwest deposits are located on the western half of the crater and all have an H-parameter value of ~0.1, which is similar to the western crater floor and typical of mature highlands regolith. The east, southeast, and south–southeast deposits are located within the boundaries of the ray and they have an H-parameter value of 0.08, which is the same as the eastern crater floor.

That the eastern pyroclastic deposits exhibit similar thermal inertia as the surrounding area is unsurprising since impact craters and rays greatly influence the thermal inertia of the lunar surface. The eastern pyroclastic deposits and crater floor are both covered with small secondary craters inside of the ray and this likely caused both areas to exhibit similar thermal inertia values. However, the western pyroclastic deposits that are not affected by the ray also exhibit similar thermal inertia as the surrounding area. This implies that the physical characteristics of the pyroclastic deposits within Oppenheimer crater are not necessarily similar to the regional deposits that contain fine-grained, spherical beads and exhibit low thermal inertia values.

There are several possible explanations for these results. A deposit emplaced by a Vulcanian-style eruption will contain blocks and ash, which would raise its thermal inertia. If an eruption began with a Vulcanian-style eruption and then finished with fire fountaining activity, the blocky, high thermal inertia material from the Vulcanian eruption could cancel out the effects of the fine-grained, low thermal inertia material from the fire fountaining activity. However, this scenario is likely to coincidental to be a reasonable solution. An alternate explanation is that if a deposit was emplaced by a Hawaiian-style eruption in which individual pyroclasts were still warm when they were deposited, the pyroclasts would have been welded together. These welded pyroclasts would have the effect of raising the thermal inertia of a deposit. A final explanation is localized deposits are small enough that over time impact gardening homogenized each deposit so that it has the same thermal properties as the surrounding regolith. The impact gardening must not affect the mineralogy of the deposits, as we observe clear differences in mineralogy between the pyroclastic deposits and the crater floor.

6.3.2. Composition

The CF values of the pyroclastic deposits (8.25–8.48 μm) range from being consistent with pyroxene to olivine or iron-rich glass. The average CF value may correlate with the size of the deposit, with the larger deposits (south, southwest, and northwest) exhibiting higher CF values and the smaller deposits (north, east, southeast, south–southeast) exhibiting lower CF values. However, this could also be due to the low CF crater ray covering the eastern half of the crater and mixing with the pyroclastic material to lower the deposits' CF value. The Clementine color ratio image (Fig. 3d) shows the extent of the crater ray. The ray covers the east, southeast and south–southeast deposits, but it does not extend to the north deposit. The north deposit has a slightly higher CF value than the east, southeast, and south–southeast deposits (8.27 μm *vs*. 8.24–8.25 μm). This implies that the east, southeast, and south–southeast deposits could be mixed with fresh material that lowers each deposit's CF value. However, the difference in CF values between the north deposit and the east, southeast, and south–southeast deposits is within the standard deviation of the measurements (±0.03–0.04 μm), so the variation between these deposits could also be due to noise. The larger deposits (south, southwest, and northwest) have CF values that range from 8.29 to 8.36 μm, although small areas within each deposit exhibit CF values as high as 8.48 μm. We interpret these values to represent an iron-rich glass, as olivine is not supported by our M^3 analyses. Most of the smaller deposits (east, southeast, and south–southeast) are homogeneous and do not exhibit areas of enhanced CF values. However the north deposit shows higher CF values in the center of the deposit and lower CF values towards the edges, which suggests a radial mixing of crater floor material with pyroclastic material.

Table 1 also shows the estimated iron abundance of each deposit. The high CF areas within the larger deposits have estimated iron abundances of up to 30 wt%. The relationship between iron abundance and CF values was calculated using Apollo samples, and in that study the sample with the highest iron abundance was Taurus Littrow (22.7 FeO wt%; Allen et al., 2012). Therefore, the nature of the relationship between iron abundance and CF value can only be extrapolated linearly above 22.7 FeO wt%. The pyroclastic glass beads from the Apollo samples have FeO contents that range from 16.5 to 24.7 wt% (Delano et al., 1986). If the linear extrapolation above 22.7 FeO wt% is an accurate representation of the iron and CF correlation, the northwest and south deposits both have areas of enhanced FeO content that contain more FeO than any other previously known lunar pyroclastic glass (∼30 wt% and ∼26 wt%, respectively). The M^3 data support the presence of glass in these deposits (Fig. 4), and therefore these deposits may contain the most iron-rich pyroclastic glass thus far identified on the Moon. SPA shows an iron-enhancement across the basin (Ohtake et al., 2014). It is possible that Oppenheimer crater's location within the iron-rich SPA basin contributed to the high iron abundances in the pyroclastic deposits. It is also possible that the thin crust in SPA basin (∼20 km as opposed to 30–50 km thick for the rest of the Moon; Wieczorek et al., 2013) meant magma sourced from the mantle spent a shorter amount of time rising through the crust and therefore had less time to accumulate less iron-rich country rock or evolve and preferentially crystallize iron-rich olivine out of the melt.

6.3.3. Classification of pyroclastic deposits based on mineralogy

Previous studies have generally studied pyroclastic deposits based on their average spectral character (*e.g.* Hawke, 1989; Gaddis et al., 2003; Jawin et al., 2015). A particular strength of this study is that we use spectral parameter maps to determine compositional and mineralogical variations at the sub-deposit level. Using these mapping techniques, we demonstrate that the mineralogy varies between and within pyroclastic deposits in Oppenheimer crater. Our results directly address the Lunar Roadmap goal of "map the extent and composition of lunar pyroclastic deposits, including their associated crystalline components" (LEAG, 2011). These mapping results show that the pyroclastic deposits within Oppenheimer crater can be divided into three groups based on their mineralogy: small glass-rich deposits, small to medium deposits that are mixtures of CPX and glass, and large deposits with complex mineralogy. Furthermore, these mineralogical groups appear to correlate with the location of the deposits within Oppenheimer crater.

In the northeastern portion of Oppenheimer crater, the small north and east deposits are both glass-rich. The north deposit exhibits the second highest glass band depths between 5% and 9%, while the east deposit exhibits the purest glass signatures (the bulk of the deposit does not appear to be significantly mixed with other minerals). Indeed, the very high 1 μm band centers in the east deposit (1.09–1.13 μm) are consistent with lab spectra of mixtures containing more than 70–80 wt% glass (Horgan et al., 2014). These deposits have CF values that lie roughly in the middle of all pyroclastic deposits, 8.27 and 8.26 μm, respectively. The mineralogy of the east deposit is shown in detail in Fig. 7. The center of this deposit is glass-rich, but the edge is a mixture of glass and crater floor material, OPX and minor CPX. While this deposit shows evidence of crater floor material mixing with juvenile material, this does not necessarily imply that it is a result of Vulcanian activity. In Vulcanian deposits, the country rock is typically mixed in with the entire deposit. Jawin et al. (2015) used M^3 data to show that some pyroclastic deposits get thinner toward the edge of the deposit and the underlying material begins to contribute to the spectral signature. Therefore it is likely that the surface material in the east deposit is entirely juvenile glassy material, and the OPX/CPX signature at the edge of the deposit is the crater floor being revealed in patches or rough terrain exposed in the thin deposit.

In the southeastern portion of Oppenheimer crater, the southeast and south–southeast deposits are mixtures of CPX and glass. These deposits have the lowest CF value of all the Oppenheimer pyroclastic deposits: both are 8.25 μm. Fig. 8 shows the detailed mineralogy and Fig. 9 shows the morphology of the southeast deposit. We observe evidence of multiple eruption centers in the southeast deposit. Fig. 9 shows two locations within the deposit that appear to be small, distinct deposits of low albedo mantling material. Thus, the southeast deposit could consist of many small eruptions that make up the larger deposit. This could explain the deposit's irregular shape, as well as some of the many vent-like craters found within the deposit.

In the western half of Oppenheimer crater, the south, southwest, and northwest deposits are all heterogeneous in composition. The south deposit contains OPX, CPX and glass, but there are sections of the deposit that are glass-rich and sections that are CPX/glass mixtures. The southwest and northwest deposits contain both CPX and glass. These three deposits exhibit the highest CF values in Oppenheimer crater, 8.28, 8.31, and 8.33 μm. While there is striping due to noise within the south deposit, there do appear to be real spectral variations between the main lobe and the eastern lobe of the deposit. These spectral variations within the deposit correspond to differences in morphology. Fig. 11 shows LROC visible images of the S deposit. The NAC image in Fig. 11b shows a glass-rich area of the deposit and the NAC image in Fig. 11c shows a CPX/glass mixture. The glass-rich area is in the center of the deposit, is smooth and flat, and does not have many large craters. In contrast, the area that is a mixture of CPX and glass is at the eastern edge of the deposit, the pyroclastic material mantles the local topography, and is associated with a crater, possibly a vent, along the fracture. Therefore, it is likely that there are at least two eruptive centers within this deposit.

6.4. Inferred eruption styles

In this section we discuss how the mineralogy of the pyroclastic deposits in Oppenheimer crater compares to the deposits drawn in Fig. 2 and how this constrains the eruption styles that likely occurred to emplace each deposit.

The first category of pyroclastic deposits (north and east deposits) in Oppenheimer crater is small and glass-rich. We hypothesize that glass-rich areas represent pyroclastic glass beads. There is no sign of mixing with plug material in these deposits, which implies that the last stage of an eruption at these vents was a fire fountaining event. If there was an initial Vulcanian eruption, the glass-rich deposit completely obscures it in both deposits.

The second category of pyroclastic deposits (southeast and south–southeast) is mixtures of CPX and glass. We hypothesize that the CPX in these pyroclastic deposits is likely crystalline juvenile material. The CPX could be sourced from the ejection of a solidified plug in a Vulcanian eruption. Alternatively, crystalline juvenile material could be emplaced if molten magma is erupted and given enough time to crystallize instead of immediately quenching and becoming glass. For example, during a high mass-eruption rate fire-fountain event in which the eruptive column is optically thick, magma droplets could crystallize (Head and Wilson, 1989). Lastly, if the eruption is a fire fountaining or Strombolian event, large blebs of molten magma can accumulate near the vent and begin to form a lava flow and crystallize. We have not directly identified lava flows associated with these pyroclastic deposits, but in the CPX-rich southeast deposit we have identified several bench craters (Fig. 9d and e). Bench craters are associated with an impact into layered terrain where less coherent materials overlie more coherent materials, such as a regolith covered mare (Oberbeck and Quaide, 1967; Quaide and Oberbeck, 1968). In the southeast deposit, bench craters might indicate that there was an impact into unconsolidated pyroclastic material or regolith overlying a lava flow. Indeed, Jozwiak et al. (2015) suggested that a lava flow could have occurred in the crater associated with the southeast deposit based on their model of floor-fractured craters. Alternatively, the bench crater could have resulted from an impact into unconsolidated pyroclastic material that overlies a more coherent crater floor material. Thus, CPX in the southeast deposit could either be plug material from multiple cycles of Vulcanian eruptions, crystalline juvenile material from less energetic fire-fountain eruptions, or from lava flows. Therefore, the eruption style of these deposits is less well constrained.

The third category of pyroclastic deposits (south, southwest, and northwest) is heterogeneous deposits. Since the composition varies throughout the deposit, it is likely that multiple eruptions created these deposits. The south deposit shows variation along the fracture, with fire fountaining likely depositing the bulk of the smooth, glass-rich pyroclastic material and Vulcanian activity depositing the smaller area that is a mixture of CPX and glassy material.

The component that is conspicuously lacking from the Oppenheimer pyroclastic deposits is country rock, or crater floor material, which is OPX-rich. As shown in Fig. 2, the presence of country rock implies there was Vulcanian activity. However, we only see OPX in one pyroclastic deposit, the south deposit, and it is likely that the OPX signatures are coming from the vent wall. Indeed, some of the strongest OPX signatures we observe are exposed in the wall of a portion of the source fracture. The lack of country rock within pyroclastic deposits in Oppenheimer crater suggests that these deposits were not emplaced by simple Vulcanian eruptions. It is still possible that there is plug material in the deposits which would support Vulcanian activity, but the lack of country rock most likely indicates that there were fire fountaining events that covered the country rock.

In summary, glass-rich deposits contain high abundances of pyroclastic glass beads, most likely emplaced in fire fountaining or Strombolian-type eruptions. CPX-rich deposits could either contain plug material from multiple cycles of Vulcanian eruptions, crystallized juvenile material from fire fountaining, or lava flows. Lastly, OPX signatures would indicate country rock/crater floor material emplaced during a classical Vulcanian eruption, but the fact that we observe very little OPX within the pyroclastic deposits suggests that they were emplaced by other types of eruptions.

6.5. Implication for magmatic activity

Vulcanian activity within a floor-fractured crater has been described in detail earlier (Head and Wilson, 1979; Head et al., 2000), but the occurrence of Vulcanian activity in association with both fire fountaining and Strombolian activity has not previously been postulated to explain glass-rich pyroclastic deposits in such a setting. This combination of eruption styles may imply variability in magma ascent rates. It has been assumed that magma ascending from sills under floor-fractured craters is rising slowly, so that the mass eruption rate is low (Head and Wilson, 1979). In a Vulcanian eruption, this leads to a cooled plug and a slow buildup of pressure beneath it. In this scenario, after the initial violent explosion the eruption would cease quickly once the overpressure is released. However, since we observe large amounts of glass-rich juvenile material, some eruption of juvenile magmatic material must have occurred. If the source magma volume was sufficiently large, the eruption mechanism could start with an initial Vulcanian eruption and then shift to a fire fountaining event Such a shift and the initial eruption could be triggered by an increase in magma ascent rate after initial plug formation.

Alternatively, the slow magma ascent rates assumed to be implied by the presence of a sill could still lead to a glass-rich deposit. If a plug does not form and magma ascends slowly to reach the surface, this could conceivably lead to relatively low mass eruption rate Strombolian activity rather than higher mass eruption rate fire fountaining. Pyroclastic glass beads in Strombolian activity are thought to be formed when bubbles within the conduit reach the surface and infinitely expand in the atmosphere-less environment, disrupting the thin surface layer of magma caught above the bubble into pyroclasts and ejecting them away from the vent (Wilson and Head, 1981). However, if these models are underestimating sill emplacement or recharge rates and the mass eruption rate of the volcanic activity within Oppenheimer crater was high, perhaps due to the thin crust at SPA, then fire fountaining could have occurred instead.

These data suggest that multiple styles of eruption, specifically both Vulcanian and fire fountaining or Strombolian activity, may have occurred within Oppenheimer crater to form the observed pyroclastic deposits. In some cases (*e.g.,* the north and east deposits) where there is a single central vent, crater floor material mixed into the deposit, and abundant glass produced by fire fountaining or Strombolian activity could have followed an initial Vulcanian eruption at the same vent. The built-up pressure from trapped gas within a sill under Oppenheimer crater could have caused the initial Vulcanian explosion and created a path to the surface for the magma. Once a pathway existed, fire fountaining or Stombolian activity would have commenced if there were enough magma still ascending through the fractures.

The possibility of multiple styles of pyroclastic eruptions may have been enhanced by the location of Oppenheimer crater within the relatively thin crust (~20 km; Wieczorek et al., 2013) of the SPA basin because of increased access to magma sources beneath the fractured crust (*e.g.*, Soderblom et al., 2015). This could have allowed fire fountaining or Strombolian activity to occur for longer periods of time as the magma was being replenished. This scenario would have resulted in larger, more iron- and glass-rich deposits in addition to the smaller Vulcanian deposits. New studies of lunar pyroclastic deposits in other geologic settings with these methods will be necessary to address these hypotheses further. Also, additional modeling work that incorporates these results is critical for understanding the ascent and eruption of magma on the Moon. This will be especially relevant at deposits like the north deposit, which has been shown to have a small cone surrounding the vent and is glass-rich. These are characteristics of a Hawaiian-style fire fountaining eruption, but the eruption occurred in a floor fractured crater setting and created a smaller deposit than has been modeled for lunar fire fountaining events. Future modeling efforts will be necessary to address the new questions raised in this study.

7. Conclusions

Our analysis of lunar pyroclastic deposits within Oppenheimer crater reveals a complex volcanic history and demonstrates the usefulness of combining mid and near infrared measurements. Our results support the following conclusions:

1. By using mapping techniques to analyze mid- and near-infrared datasets, we were able to analyze localized pyroclastic deposits in more detail than previous studies. A major result of this study was that we identified variable mineralogy within and between pyroclastic deposits in Oppenheimer crater.
2. The pyroclastic deposits within Oppenheimer contain various ratios of pyroxene (CPX and/or OPX) to iron-rich glass. All the deposits contain glass; the east and northwest deposit are the most glass-rich. Many deposits also exhibit strong CPX signatures that may be crystalline juvenile products emplaced during the pyroclastic eruptions. No olivine was identified within Oppenheimer crater, despite its location within the deep South Pole Aitkin basin.
3. The mineralogic variations between deposits result from a combination of pyroclastic Vulcanian activity (producing glass and CPX), fire fountaining or Strombolian activity (producing glass), and possible lava flows related to the latter category of eruptions (producing CPX).
4. Morphology from visible images and variable mineralogy within deposits imply that several of the deposits (south and southeast) are likely the result of multiple eruption centers.
5. The variability of eruption styles and composition inferred for these deposits suggests that the eruption mechanics of local pyroclastic eruptions and the magmatic histories of floor-fractured craters are more complicated than previously thought.
6. Oppenheimer crater's location within the SPA basin could have caused the high iron content of the deposits, and the thin crust could have enabled magma transport to the surface.
7. From a resource standpoint, the three largest pyroclastic deposits within Oppenheimer (northwest, southwest and south) would be good sites for future exploration. These deposits contain the most iron-rich volcanic glass thus far identified on the Moon (giving them a high potential to also contain significant abundances of oxygen), have large areas (the northwest deposit is large enough to be considered a regional deposit; $< 1000\,km^2$), and are not covered in impact ejecta like the deposits on the eastern half of the crater.

Acknowledgments

We would like to thank the LRO Diviner and LROC teams and the M^3 team for providing those datasets. We would also like to thank Marie McBride for the helpful discussions. Finally, we thank two anonymous reviewers for their constructive comments.

Supplementary materials

Supplementary material associated with this article can be found, in the online version, at doi:10.1016/j.icarus.2016.02.007.

References

Adams, J.B., 1974. Visible and near-infrared diffuse reflectance spectra of pyroxenes as applied to remote sensing of solid objects in the Solar System. J. Geophys. Res. 79, 4829–4836. doi:10.1029/JB079i032p04829.

Allen, C.C., Morris, R.V., McKay, D.S., 1996. Oxygen extraction from lunar soils and pyroclastic glass. J. Geophys. Res. 101 (E11), 26085–26095. doi:10.1029/96JE02726.

Allen, C.C., Greenhagen, B.T., Donaldson Hanna, K.L., et al., 2012. Analysis of lunar pyroclastic deposit FeO abundances by LRO Diviner. J. Geophys. Res. 117, 1–12. doi:10.1029/2011JE003982, E00H28.

Arndt, J., Engelhardt, W.V., Gonzalez-Cabeza, I., Meier, B., 1984. Formation of Apollo 15 green glass beads. In: Proceedings of the 15th Lunar and Planetary Science Conference, pp. C225–C232.

Arndt, J., Engelhardt, W., 1987. Formation of Apollo 17 orange and black glass beads. J. Geophys. Res. 92, E372–E376.

Bandfield, J.L., et al., 2011. Lunar surface rock abundance and regolith fines temperatures derived from LRO Diviner Radiometer data. J. Geophys. Res. 116, 1–18. doi:10.1029/2011JE003866, E00H02.

Besse, S.J., et al., 2013. A visible and near-infrared photometric correction for Moon Mineralogy Mapper (M^3). Icarus 222 (1), 229–242. doi:10.1016/j.icarus.2012.10.036.

Boardman, J.W., et al., 2011. Measuring moonlight: An overview of the spatial properties, lunar coverage, selenolocation, and related Level 1B products of the Moon Mineralogy Mapper. J. Geophys. Res. 116, 1–15. doi:10.1029/2010JE003730, E00G14.

Burns, J.O., Kring, D.A., Hopkins, J.B., et al., 2013. A lunar L2-Farside exploration and science mission concept with the Orion Multi-Purpose Crew Vehicle and a teleoperated lander/rover. Adv. Space Res. 52 (2), 306–320. doi:10.1016/j.asr.2012.11.016.

Campbell, B.A., Hawke, B.R., Morgan, G.A., 2014. Improved discrimination of volcanic complexes, tectonic features, and regolith properties in Mare Serenitatis from Earth-based radar mapping. J. Geophys. Res.: Planets 119, 313–330. doi:10.1002/(ISSN)2169-9100.

Carter, L.M., Campbell, B.A., Hawke, B.R., et al., 2009. Radar remote sensing of pyroclastic deposits in the southern Mare Serenitatis and Mare Vaporum regions of the Moon. J. Geophys. Res. 114 (E11), 1–12. doi:10.1029/2009JE003406, E11004.

Christensen, P.R., Engle, E., Anwar, S., et al., 2009. JMARS – A planetary GIS. In: Proceedings of the AGU Fall Meeting, Abstract #IN22A-06.

Clark, R., Roush, T., 1984. Reflectance spectroscopy: Quantitative analysis techniques for remote sensing applications. J. Geophys. Res. 89, 6329–6340.

Clark, R.N., Pieters, C.M., Green, R.O., et al., 2011. Thermal removal from near-infrared imaging spectroscopy data of the Moon. J. Geophys. Res. 116, 1–9. doi:10.1029/2010JE003751, E00G16.

Cloutis, E.A., Gaffey, M.J., 1991. Spectral-compositional variations in the constituent minerals of mafic and ultramafic assemblages and remote sensing implications. Earth Moon Planets 53, 11–53. doi:10.1007/BF00116217.

Delano, J.W., 1986. Pristine lunar glasses: Criteria, data, and implications. J. Geophys. Res. 16, D201–D213.

Dundas, C.M., McEwen, A.S., 2007. Rays and secondary craters of Tycho. Icarus 186 (1), 31–40. doi:10.1016/j.icarus.2006.08.011.

Gaddis, L.R., Pieters, C.M., Ray Hawke, B., 1985. Remote sensing of lunar pyroclastic mantling deposits. Icarus 61 (3), 461–489.

Gaddis, L.R., Hawke, B.R., Robinson, M.S., et al., 2000. Compositional analyses of small lunar pyroclastic deposits using Clementine multispectral data. *J. Geophys. Res.* 105 (E2), 4245–4262.

Gaddis, L.R., Staid, M.I., Tyburczy, J.A., et al., 2003. Compositional analyses of lunar pyroclastic deposits. Icarus 161 (2), 262–280. doi:10.1016/S0019-1035(02)00036-2.
Gaddis, L.R., Weller, L., Barret, J., et al., 2013. "New" volcanic features in lunar floor-fractured Oppenheimer crater. In: Proceedings of the 44th Lunar and Planetary Science Conference, p. p. 2262.
Glotch, T.D., Lucey, P.G., Bandfield, J.L., et al., 2010. Highly Silicic Compositions on the Moon. Science 329 (5998), 1510–1513. doi:10.1126/science.1192148.
Green, R.O., Pieters, C., Mouroulis, P., et al., 2011. The Moon Mineralogy Mapper imaging spectrometer for lunar science: Instrument description, calibration, on-orbit measurements, science data calibration and on-orbit validation. J. Geophys. Res. 116, 1–31. doi:10.1029/2011JE003797, E00G19.
Greenhagen, B.T., Lucey, P.G., Wyatt, M.B., et al., 2010. Global silicate mineralogy of the Moon from the Diviner Lunar Radiometer. Science 329 (5998), 1507–1509. doi:10.1126/science.1192196.
Gustafson, J.O., Bell III, J.F., Gaddis, L.R., et al., 2012. Characterization of previously unidentified lunar pyroclastic deposits using Lunar Reconnaissance Orbiter Camera data. J. Geophys. Res. 117 (E12), 1–21. doi:10.1029/2011JE003893, E00H25.
Hauri, E.H., Weinreich, T., Saal, A.E., et al., 2011. High pre-eruptive water contents preserved in lunar melt inclusions. Science 333 (6039), 213–215. doi:10.1126/science.1204626.
Hauri, E.H., Saal, A.E., Rutherford, M.J., et al., 2015. Water in the Moon's interior: Truth and consequences. Earth Planet. Sci. Lett. 409 (C), 252–264. doi:10.1016/j.epsl.2014.10.053.
Hawke, B.R., Coombs, C.R., Gaddis, L.R., et al., 1989. Remote sensing and geologic studies of localized dark mantle deposits on the moon. In: Proceedings of the 20th Lunar and Planetary Science Conference, pp. 255–268.
Hawke, B.R., Coombs, C.R., Clark, B., 1990. Ilmenite-rich pyroclastic deposits: An ideal lunar resource. In: Proceedings of the 20th Lunar and Planetary Science Conference, pp. 249–258.
Hawke, B.R., Blewett, D.T., Lucey, P.G., et al., 2004. The origin of lunar crater rays. Icarus 170 (1), 1–16. doi:10.1016/j.icarus.2004.02.013.
Head, J.W., 1974. Lunar dark-mantle deposits – Possible clues to the distribution of early mare deposits. In: Proceedings of the 5th Lunar and Planetary Science Conference, pp. 207–222.
Head III, J.W., Wilson, L., 1979. Alphonsus-type dark-halo craters – Morphology, morphometry and eruption conditions. In: Proceedings of the 5th Lunar and Planetary Science Conference, pp. 2861–2897.
Head, J.W., Wilson, L., 1989. Basaltic pyroclastic eruptions: influence of gas-release patterns and volume fluxes on fountain structure, and the formation of cinder cones, spatter cones, rootless flows, lava ponds and lava flows. J. Volcan. Geoth. Res. 37 (3), 261–271.
Head III, J.W., Wilson, L., Pieters, C.M., 2000. Pyroclastic eruptions associated with the floor-fractured lunar farside crater Oppenheimer in the South Pole Aitken Basin. In: Proceedings of the 31st Lunar and Planetary Science Conference, p. 1280.
Heiken, G.H., McKay, D.S., Brown, R.W., 1974. Lunar deposits of possible pyroclastic origin. Geochim. Cosmochim. Acta 38, 1703–1718.
Hicks, M.D., Buratti, B.J., Nettles, J., et al., 2011. A photometric function for analysis of lunar images in the visual and infrared based on Moon Mineralogy Mapper observations. J. Geophys. Res. 116 (E12), E00G15. doi:10.1029/2010JE003733.
Hiesinger, H., Jaumann, R., Neukum, G., et al., 2000. Ages of mare basalts on the lunar nearside. J. Geophys. Res. 105 (E12), 29239–29275. doi:10.1029/2000JE001244.
Hiesinger, H., Van Der Bogert, C.H., Jolliff, B.L., et al., 2012. Stratigraphy of the South Pole–Aitken Basin based on crater size-frequency distribution measurements. In: Proceedings of the GSA Annual Meeting, GSA #30953-212430.
Horgan, B.H.N., Cloutis, E.A., Mann, P., et al., 2014. Near-infrared spectra of ferrous mineral mixtures and methods for their identification in planetary surface spectra. Icarus 234 (C), 132–154. doi:10.1016/j.icarus.2014.02.031.
Jawin, E.R., Besse, S., Gaddis, L.R., et al., 2015. Examining spectral variations in localized lunar dark mantle deposits. J. Geophys. Res.: Planets 120, 1310–1331. doi:10.1002/2014JE004759.
Jozwiak, L.M., Head, J.W., Wilson, L., 2015. Lunar floor-fractured craters as magmatic intrusions: Geometry, modes of emplacement, associated tectonic and volcanic features, and implications for gravity anomalies. Icarus 248 (C), 424–447. doi:10.1016/j.icarus.2014.10.052.
Klima, R.L., Dyar, D.M., Pieters, C.M., 2011. Near-Infrared spectra of clinopyroxenes: Effects of calcium content and crystal structure. Meteor. Planet. Sci. 46, 379–395. doi:10.1111/j.1945-5100.2010.01158.
Lunar Exploration Analysis Group, 2011. The Lunar Exploration Roadmap: Exploring the Moon in the 21st Century: Themes, Goals, Objectives, Investigations, and Priorities. Lunar Exploration Analysis Group.
McEwen, A.S., Robinson, M.S., 1997. Mapping of the Moon by Clementine. Adv. Space Res. 19 (10), 1523–1533.
Nozette, S., 1995. The Clementine mission: Past, present, and future. Acta Astronautica 35 (Suppl. 1), S161–S169. doi:10.1016/0094-5765(94)00181-K.
Oberbeck, V.R., Quaide, W.L., 1967. Estimated thickness of a fragmental surface layer of Oceanus Procellarum. J. Geophys. Res 72 (18), 4697–4704.
Ohtake, M., Uemoto, K., Yokota, Y., et al., 2014. Geologic structure generated by large-impact basin formation observed at the South Pole–Aitken basin on the Moon. Geophys. Res. Lett. 41 (8), 2738–2745. doi:10.1002/(ISSN)1944-8007.
Paige, D.A., Foote, M.C., Greenhagen, B.T., et al., 2009. The Lunar Reconnaissance Orbiter Diviner Lunar Radiometer Experiment. Space Sci. Rev. 150 (1–4), 125–160. doi:10.1007/s11214-009-9529-2.
Petro, N.E., Gaddis, L.R., Staid, M.I., 2001. Analysis of the Oppenheimer pyroclastic deposits using Clementine UVVIS data. LPSC 32 #1953.
Pieters, C.M., McCord, T.B., Charette, M.P., et al., 1974. Lunar surface: Identification of the dark mantling material in the Apollo 17 soil samples. Science 183, 1191–1194.
Pieters, C.M., Boardman, J., Buratti, B., et al., 2009. The Moon mineralogy mapper (M^3) on Chandrayaan-1. Curr. Sci 96 (4), 500–505.
Quaide, W.L., Oberbeck, V.R., 1968. Thickness determinations of the lunar surface layer from lunar impact craters. J. Geophys. Res. 73 (16), 5247–5270.
Robinson, M.S., Brylow, S.M., Tschimmel, M., et al., 2010. Lunar Reconnaissance Orbiter Camera (LROC) instrument overview. Space Sci. Rev. 150 (1–4), 81–124.
Schultz, P.H., 1976. Floor-fractured lunar craters. Moon 15 (3–4), 241–273.
Shearer, C.K., Papike, J.J., 1993. Basaltic magmatism on the Moon: A perspective from volcanic picritic glass beads. Geochim. Cosmochim. Acta 57 (19), 4785–4812. doi:10.1016/0016-7037(93)90200-G.
Smith, D.E., Zuber, M.T., Jackson, G.B., et al., 2010. The Lunar Orbiter Laser Altimeter investigation on the Lunar Reconnaissance Orbiter Mission. Space Sci. Rev. 150 (1–4), 209–241. doi:10.1007/s11214-009-9512-y.
Soderblom, J.M., Evans, A.J., Johnson, B.C., et al., 2015. The fractured Moon: Production and saturation of porosity in the lunar highlands from impact cratering. Geophys. Res. Lett. 42, 6939–6944.
Sunshine, J.M., Pieters, C.M., 1993. Estimating modal abundances from the spectra of natural and laboratory pyroxene mixtures using the modified Gaussian model. J. Geophys. Res. 98 (E5), 9075–9087.
Trang, D., Lucey, P.G., Gillis-Davis, J.J., et al., 2013. Near-infrared optical constants of naturally occurring olivine and synthetic pyroxene as a function of mineral composition. J. Geophys. Res.: Planets 118, 708–732. doi:10.1002/jgre.20072.
Vasavada, A.R., Bandfield, J.L., Greenhagen, B.T., et al., 2012. Lunar equatorial surface temperatures and regolith properties from the Diviner Lunar Radiometer Experiment. Journal of Geophysical Research 117, 1–12. doi:10.1029/2011JE003987, E00H18.
Wieczorek, M.A., Neumann, G.A., Nimmo, F., et al., 2013. The crust of the Moon as seen by GRAIL. Science 339, 671–675. doi:10.1126/science.1231530.
Wilhelms, D.E., 1987. The Geologic History of the Moon. United States Geological Survey Professional Paper 1348.
Wilson, L., Head III, J.W., 1981. Ascent and eruption of basaltic magma on the Earth and Moon. J. Geophys. Res. 86 (B4), 2971–3001.